Boundary Conditions for 3D Fluid-Structure Interaction Simulations of Compliant Vessels

Merethe Sirevåg Hansen

Assignment

A 3D straight tube (fluid and solid) should be modelled and may be tested
with the following boundary conditions at the outlet:

i) Zero reflection (Absorbing)

ii) Two- and/or three-element Windkessel model

iii) Network model

A fluid structure interaction simulation should be run on all cases, using
Abaqus (solid), Fluent (fluid) and Tango (coupling). The influence of grid
refinement and the CFL-condition should be investigated. For the solid part,
the effect of using shell elements instead of 3D-elements should be looked
at. A possibility is to use Pyformex for grid generation. As an extension
the same boundary conditions may be tested on an idealized aortic arch
geometry, and further a patient specific geometry.

Preface

This report describes the work done in my Master thesis, as a conclusion of my 5-year M. Sc. program in Mechanical Engineering at NTNU, at the Department of Structural Engineering. The goal of the study was to investigate boundary conditions for a straight compliant tube, related to blood flow in the aorta, by the means of fluid-structure interaction simulations.

I would like to thank my supervisor, Leif Rune Hellevik, for guidance and help through the project, and my co-supervisor, Paul Roger Leinan, for help with solving technical problems that occurred when running simulations. I would also like to thank last year's master student on this subject, Thomas Bertheau Eeg, for letting me use his work as a basis for this study, and my room mate, Lin Gunhild Bruvoll, for proof reading this report.

Merethe S. Hansen

Merethe Sirevåg Hansen
June 7, 2012
Trondheim, Norway

Sammendrag

Målet med denne studien var å undersøke ulike utløpsgrensebetingelser for et rett, elastisk rør, ved hjelp av fluid-struktur-interaksjonssimuleringer. I tillegg til å se på grensebetingelser, var det ønskelig å se hvordan forskjellige parametre, som tidsskritt, cellestørrelse og CFL-tall ville påvirke resultatene. Det ble kjørt simuleringer med forskjellige tidsskritt og nett. Det hadde liten innvirkning på resultatene å forandre disse parametrene, bortsett fra når tidsskrittene var veldig små. Da ville ikke simuleringene konvergere. Fire ulike grensebetingelser ble testet på utløpet: refleksjonsfri rand, en gitt refleksjonsfaktor på $\Gamma = 0.9$, og to- og treelements Windkesselmodeller. Den refleksjonsfrie modellen gav nesten ingen refleksjoner, mens simuleringen der refleksjonsfaktoren var satt til $\Gamma = 0.9$ på utløpet gav den gitte mengden refleksjoner. For det refleksjonsfrie tilfellet var resultatene unøyaktige sammenlignet med enklere analytiske løsninger, fordi antakelsen om Poiseuille-strømning var ugyldig. Nøyaktigheten økte da hastighetsprofilet ble endret fra uniformt til parabolsk. Det var ikke mulig å modellere en refleksjonsfri rand med en to-elements Windkesselmodel. Refleksjoner oppstod også når parametrene var valgt slik at de teoretisk sett ikke skulle ha gitt refleksjoner. Dette kunne bedres ved å bruke en tre-elements Windkesselmodel. Da ble mengden refleksjoner veldig liten hvis parametrene ble valgt slik at det teoretisk sett ikke skulle oppstå refleksjoner.

Abstract

The goal of this study was to investigate different outlet boundary conditions for a straight compliant tube, by the means of fluid-structure interaction simulations. In addition to investigating boundary conditions it was desirable to see how different parameters, like time step, grid refinement and CFL-number would influence the results. Simulations were run with different time steps and grids. Changing these parameters had only minor influence on the results of the simulations, except for very small time steps, when the simulations would not converge. Four different boundary conditions were tested at the outlet: A reflection free boundary, an imposed reflection factor of $\Gamma = 0.9$, a two-element Windkessel model and a three-element Windkessel model. The reflection free model gave almost no reflections, while the simulation with a reflection factor of $\Gamma = 0.9$ gave the imposed amount of reflections at the outlet. For the reflection free case, comparing the results with simpler, analytical solutions gave poor accuracy, because the assumption of Poiseuille flow was invalid. Changing the velocity profile at the inlet from uniform to parabolic improved the accuracy. The two-element Windkessel model was not able to model a reflection free outlet. Reflections would occur even when the parameters were chosen to give a theoretically reflection free outlet. This was improved by using the three-element Windkessel model. When choosing parameters that would theoretically give zero reflections, the amount of reflections was very low.

Contents

I Abbreviations

ALE	Arbitrary Lagrangian Eulerian
CFD	Computational Fluid Dynamics
FDM	Finite Difference Method
FEA	Finite Element Analysis
FEM	Finite Element Method
FSI	Fluid-Structure Interaction
FVM	Finite Volume Method

II Nomenclature

Angular frequency	ω	Pressure	p
Area	A	Pulse wave velocity	c_0
Body force	$\mathbf{b}$	Radius	r
CFL-number	CFL	Reflection factor	Γ
Characteristic impedance	Z_c	Residual	$\mathbf{R}$
Compliance	C	Resistance	R
Damping coefficient	γ_d	Reynolds number	Re
Density	ρ	Shear stress	τ_0
Diameter	D	Solid boundary	Γ_s
Displacement	$\mathbf{u}$	Solid sub-domain	Ω_s
Flow solver	$\mathbf{F}$	Strain rate tensor	$\mathbf{D}$
Fluid boundary	Γ_f	Stress tensor	$\mathbf{T}$
Fluid sub-domain	Ω_f	Structural solver	$\mathbf{S}$
Fluid-structure interface	Γ_i	Terminal impedance	Z_T
Frequency	f	Thickness	h
Green strain tensor	$\mathbf{E}$	Time	t
Identity matrix	$\mathbf{I}$	Time constant	τ
Imaginary unit	j	Total arterial compliance	C_V
Input impedance	Z_{in}	Velocity	$\mathbf{v}$
Jacobian matrix	$\mathbf{R}'$	Viscosity	μ
Normal stress	σ	Volume	V
Normal vector	$\mathbf{n}$	Volume flow	Q
Poisson's ratio	ν	Young's modulus	E

1 Introduction

For many engineering problems the influence of the surrounding fluid on the displacements of a structure is negligible, and the dynamics of a structure has negligible influence on the flow and pressure fields of a fluid. Nevertheless, in some cases this interaction is not negligible. The flow of an incompressible fluid in a compliant tube is one such case. A physical example of this is blood flow in arteries. The deformation of the compliant blood vessels influences the blood pressure, and the pressure of the fluid determines how the blood vessels deform. A coupling between the fluid and the structure is needed to model the propagation of the pressure and flow waves that occur in the cardiovascular system.

Cardiovascular diseases are the main cause of death in developed countries [7, p.36]. The World Health Organization has estimated that about 30 % of all deaths globally in 2008 were due to diseases in the cardiovascular system [16]. Good understanding of the mechanics of the human cardiovascular system can be of great help when it comes to predicting and preventing cardiovascular diseases.

Fluid-structure interaction (FSI) simulations make it possible to accurately model blood flow in arteries. FSI-simulations are very computational expensive though, so simplifications have to be made. A necessary simplification to reduce the computational cost, is to divide the cardiovascular system into smaller parts and look at one part at a time. To make such a simplification valid, boundary conditions that give a good representation of the rest of the cardiovascular system are crucial.

In this study boundary conditions for blood flow through a straight, compliant tube are investigated. Using a straight tube is a very basic approach, but there are many factors that can affect the results of the simulations, even for a very simple geometry. If the results from a simple analysis are not reliable, they certainly will not be for more advanced models. Therefore, in addition to testing different boundary conditions, it will be investigated how different meshes and time steps influence the results of a simulation. As far as it is possible, the results will be compared to the analytical solution of similar but more simplified problems, to see if they are physical or not. It is also interesting to see how different boundary conditions are able to model wave reflections.

This report is organized as follows: In chapter 2 all relevant theory is presented. This includes governing equations, the analytical solutions of some simple, relevant cases, the mathematics behind the boundary conditions that will be tested and some general information about FSI-simulations and the software used in this study. Parts of this chapter[1] is based on the report from the pre-project for this thesis that was written by the author in the fall

---

[1]Sections 2.1, 2.2.1, 2.2.2, 2.3, 2.4, 2.5.1, and 2.5.2.

of 2012 [8]. In chapter 3 all the cases for the simulations are presented with geometry, meshes, material properties and boundary conditions, before the results are presented and discussed in chapter 4.

2 Theory

2.1 Physiology

The cardiovascular system consists of the heart and the blood vessels. The heart is mainly built up of myocardium, which is a type of muscle cell that has lower contractability and much higher resistance to fatigue than the other muscles in the body [7, p. 3]. It has four chambers: the left and right atria on top, and the left and right ventricles at the bottom. The left ventricle is where the blood is pumped through the aortic valve and into the aorta.

The blood vessels distribute oxygenated blood to the body and bring deoxygenated blood back to the heart. The system can be divided into two parts; the pulmonary system, which consists of the right part of the heart and the blood vessels that distribute and collect blood to and from the lungs, and the systemic system, which consists of the left part of the heart and the network of vessels that bring blood to and from the micro circulation in the rest of the body. The systemic system consists of blood vessels with three different tasks. The arteries carry blood from the heart to the body and the veins carry the blood back to the heart. The capillaries or the microcirculation carry out exchange processes with other tissue. The diameter of the blood vessels vary from about 0.006 mm to 0.01 mm for the capillaries, to roughly 25 mm for the aorta and 30 mm for the vena cava [7, p. 6]. The aorta is the artery closest to the heart.

The walls of the large arteries have three layers: the intima (internal layer), the media, and the adventitia (external layer). The channel for blood flow inside the vessel is called the lumen, and the interface between the flowing blood and the vessel wall is called the endothelium. Some of the tasks of the endothelium are to control the blood-wall exchange and regulation of blood coagulation. The endothelial cells are subjected to normal stresses from the blood pressure, shear stresses resulting from friction of the flowing blood, and circumferential tension from neighbouring cells. Blood vessels are compliant, so the area of the vessel varies with the pressure pulse of the flow.

Blood consists of cells and plasma. The plasma takes up about 55 % of the blood volume, and the main ingredient in blood plasma is water (approximately 92 %) [7, p. 22]. The volume fraction of blood cells is called haematocrit. There are three main groups of blood cells: erythrocytes, leukocytes and platelets. The erythrocytes (red blood cells) are the largest group and takes up 97 % of the cell volume [7, p. 22]. Together with the blood plasma they determine the mechanical properties of blood. The leukocytes (white blood cells) are involved in the immune defence of the body, and the platelets or thrombocytes are involved in blood coagulation.

There are two steps in the cardiac cycle: systole and diastole. Systole

is the period when the heart contracts and blood is ejected from the left ventricle into the aorta (and similarly for the right side of the heart), and diastole is the period when the heart relaxes. The arterial blood pressure can be defined similarly; it varies between systolic (maximum) and diastolic (minimum) pressure.

2.2 Fluid Model

2.2.1 Governing Equations

The governing equations in fluid dynamics are the equation of mass conservation and the Navier-Stokes equations. For an incompressible, Newtonian fluid these are given by Eqs. (1) and (2) respectively:

$$\nabla \cdot \mathbf{v} = 0 \tag{1}$$

$$\frac{\partial \mathbf{v}}{\partial t} + (\mathbf{v} \cdot \nabla)\mathbf{v} = -\frac{1}{\rho}\nabla p + \frac{\mu}{\rho}\nabla^2 \mathbf{v} + \mathbf{b} \tag{2}$$

where $\mathbf{v}$ is the velocity vector, p is the pressure, ρ is density, μ is viscosity and $\mathbf{b}$ is a vector of body forces.

2.2.2 Material Model

In 1687 Sir Isaac Newton postulated the following relationship between the shear stress and the velocity gradient for 1D fluid flow [15, p. 26]:

$$\tau_0 = \mu\frac{dv_x}{dy} \tag{3}$$

Equation (3) can be generalized to [10, p. 326]:

$$\mathbf{T} = -p\mathbf{I} + 2\mu\mathbf{D} \tag{4}$$

for incompressible fluids, where $\mathbf{T}$ is the stress tensor, $\mathbf{I}$ is the identity matrix and $\mathbf{D}$ is the strain rate tensor. This is the material model for a Newtonian fluid, and the constitutive equation that is used in the Navier-Stokes equations.

2.2.3 The CFL- and the Reynolds number

The CFL-number is an important dimensionless number for determining whether or not a numerical computation is stable. It is defined as:

$$\text{CFL} = \frac{c_0\Delta t}{\Delta x} \tag{5}$$

where c_0 is the speed with which disturbances propagate, Δt is the time step and Δx is the grid size. For most of the conditionally stable Finite Volume Method-schemes (see chapter 2.5.1) the stability condition is:

$$|\text{CFL}| \leq 1 \tag{6}$$

A physical interpretation of the CFL-number is that disturbances should not propagate over a distance longer then the size of the cell during one time step.

The Reynolds number is a ratio between inertial and viscous forces. For pipe flow it is defined as:

$$Re = \frac{\rho v_0 D}{\mu} \tag{7}$$

where D is the diameter of the pipe, and v_0 is the mean velocity. The Reynolds number is used to define the transition from laminar to turbulent flow. For circular pipe flow the accepted critical Reynolds number for transition to turbulent flow is $Re_{D,crit} \approx 2300$ [15, p. 342].

2.2.4 Transient flow in One-Dimensional Stiff Tubes

Assuming one-dimensional flow where the velocity $v_x = v_x(t)$ is a function of time only, the Navier-Stokes equations are reduced to:

$$\frac{\partial p}{\partial x} = -\rho \frac{dv_x}{dt} \tag{8}$$

For a velocity that is varying as a squared sine wave in time, $v_x = B \sin^2(\pi f t)$, where B is the amplitude of the velocity wave and f is the frequency, the pressure gradient is given as:

$$\frac{\partial p}{\partial x} = -\pi B f \rho \sin(2\pi f t) \tag{9}$$

or:

$$p_{in} = p_{out} + \pi B f \rho L \sin(2\pi f t) \tag{10}$$

where L is the length of the tube.

2.2.5 Pulsatile Flow in One-Dimensional Compliant Tubes

In compliant tubes the cross-sectional area of the tube A, depends on the pressure. The compliance C is defined as:

$$C = \frac{\partial A}{\partial p} \tag{11}$$

The area change with time has to be taken into account in the continuity and momentum equation. For one-dimensional flow of an incompressible, Newtonian fluid, and with the volume flow Q as the flow variable, Eqs. (1) and (2) can be written as [9, ch. 8]:

$$\frac{\partial A}{\partial t} + \frac{\partial Q}{\partial x} = 0 \tag{12}$$

$$\frac{\partial Q}{\partial t} + \frac{\partial}{\partial x}(\frac{Q^2}{A}) = -\frac{A}{\rho}\frac{\partial p}{\partial x} + \frac{\pi D}{\rho}\tau_0 \tag{13}$$

respectively, where x is the stream wise direction, D is the diameter of the tube and τ_0 is the shear stress. The friction term depends on the local velocity profile, but assuming fully developed Poiseuille flow the shear stress is given by:

$$\tau_0 = \frac{8\mu Q}{DA} \tag{14}$$

The linearized version of the momentum equation, (13), then becomes:

$$\frac{\partial Q}{\partial t} = -\frac{A}{\rho}\frac{\partial p}{\partial x} + \frac{8\pi\mu Q}{\rho A} \tag{15}$$

Using the definition of the compliance C and the pulse wave velocity $c_0^2 = \frac{1}{C}\frac{A}{\rho}$, the area can be eliminated from Eqs. (12) and (15):

$$\frac{\partial p}{\partial t} = -\frac{1}{C}\frac{\partial Q}{\partial x} \tag{16}$$

$$\frac{\partial Q}{\partial t} = -c_0^2 C\frac{\partial p}{\partial x} + bQ \tag{17}$$

where $b = \frac{8\pi\mu}{\rho A}$. Cross-derivation and subtraction give the wave equations with damping for pressure and flow:

$$\frac{\partial^2 p}{\partial t^2} - c_0^2\frac{\partial^2 p}{\partial x^2} + \frac{b}{C}\frac{\partial Q}{\partial x} = 0 \tag{18}$$

$$\frac{\partial^2 Q}{\partial t^2} - c_0^2\frac{\partial^2 Q}{\partial x^2} - b\frac{\partial Q}{\partial t} = 0 \tag{19}$$

For inviscid flow ($b = 0$), Eqs. (18) and (19) are reduced to the standard wave equations.

The Moens-Korteweg formula for the pulse wave velocity

The Moens-Korteweg formula relates the pulse wave velocity to the geometrical and material properties of a tube and the flow in it. It is derived from Hooke's law:

$$\Delta\sigma_\theta = E\frac{dr}{r} \tag{20}$$

where $\Delta\sigma_\theta$ is the change in circumferential stress, E is the Young's modulus and r is the radius of the tube. For small deformations the following relations between pressure and stress applies before and after deformation:

$$\sigma_{\theta 1} = \frac{pr}{h} \tag{21}$$

$$\sigma_{\theta 2} \approx \frac{(p+dp)r}{h} \tag{22}$$

where h is the thickness of the tube. Combining the expressions for σ_θ gives:

$$\frac{dp}{dA} = \frac{Eh}{2Ar} \tag{23}$$

which is the inverse of the compliance. Substitution into the definition of the pulse wave velocity, the Moens-Korteweg formula is obtained [9, ch. 8]:

$$c_0 = \sqrt{\frac{Eh}{2\rho r}} \tag{24}$$

Analytical solution of the wave equations with damping

Equations (18) and (19) can be solved by proposing a solution on the form:

$$Q = Q_0 e^{j\omega(t-\frac{x}{k})} \tag{25}$$

$$p = p_0 e^{j\omega(t-\frac{x}{k})} \tag{26}$$

where j is the imaginary unit $j = \sqrt{-1}$, ω is the angular frequency and k is the wave speed with damping. Derivating and inserting into Eqs. (18) and (19), the following characteristic equations are established:

$$\omega^2 - (\frac{c_0\omega}{k})^2 + jb\omega = 0 \tag{27}$$

$$p_0\omega^2 - (\frac{c_0\omega}{k})^2 + j\frac{b\omega}{Ck}Q_0 = 0 \tag{28}$$

rewriting Eq. (27) gives an expression for k^2:

$$k^2 = \frac{(c_0\omega)^2}{\omega^2 + jb\omega} \tag{29}$$

Writing Eq. (29) on polar form and taking the square root gives:

$$k = \pm c_0 (1 + (\frac{b}{\omega})^2)^{-\frac{1}{4}} e^{-j\frac{\phi}{2}} \tag{30}$$

where $\phi = \arctan(\frac{b}{\omega})$, or:

$$|k| = c_0 (1 + (\frac{b}{\omega})^2)^{-\frac{1}{4}} \tag{31}$$

$$k_r = |k| \cos(\frac{\phi}{2}) \tag{32}$$

$$k_i = |k| \sin(\frac{\phi}{2}) \tag{33}$$

where k_r is the real part of k and k_i is the imaginary part of k.

Now that k is known, the damping term in Eq. (25) can be established:

$$\mp j\frac{\omega}{k} = \pm \frac{\omega}{|k|} \sin(\frac{\phi}{2}) \mp j\frac{\omega}{|k|} \cos(\frac{\phi}{2}) \tag{34}$$

A necessary condition for damping to be present is that the real part of Eq. (34) is negative. The solution then becomes:

$$Q = Q_0 e^{j\omega t} e^{-\gamma_d x} \tag{35}$$

where $\gamma_d = \frac{\omega}{|k|} \sin(\frac{\phi}{2})$ is the damping coefficient. By using the definition of the angle ϕ, the expression for γ_d can be rewritten to:

$$\gamma_d = \frac{b}{2c_0}(1 + (\frac{b}{\omega})^2)^{\frac{3}{4}} \tag{36}$$

so the damping coefficient is independent of frequency for $b/\omega << 1$. Writing out the expression for b and using the Moens-Korteweg formula for c_0 it becomes clear that γ_d is a function of geometry and material properties only, for $b/\omega << 1$:

$$\gamma_d = \frac{\mu}{D\sqrt{\rho E h D}} \tag{37}$$

where D is the diameter and h is the thickness of the tube.

Characteristic and input impedance

For the inviscid form of Eqs. (18) and (19), a solution on the following form can be suggested [9, ch. 8]:

$$p = p_0 f(x - ct) + p_0^* g(x + c_0 t) \tag{38}$$

$$Q = Q_0 f(x - ct) + Q_0^* g(x + c_0 t) \tag{39}$$

where f and g are waves travelling forward and backward respectively, with wave speed c_0. Inserting into the inviscid version of Eq. (15),

$$\frac{\partial Q}{\partial t} = -\frac{A}{\rho}\frac{\partial p}{\partial x} \tag{40}$$

gives:

$$f'(p_0\frac{A}{\rho} - Q_0 c_0) + g'(p_0^*\frac{A}{\rho} + Q_0^* c_0) = 0 \tag{41}$$

This has to be valid for arbitrary functions f and g, so:

$$Z_c = \frac{p_0}{Q_0} = \frac{\rho c_0}{A} = -\frac{p_0^*}{Q_0^*} \tag{42}$$

have to be true. Z_c is called the characteristic impedance of the flow, and is a relation between pressure and flow for a unidirectional wave. The characteristic impedance can also be expressed in terms of geometrical and material parameters, by using the Moens-Korteweg formula for the pulse wave velocity:

$$Z_c = \sqrt{\frac{\rho E h}{A^2 D}} \tag{43}$$

Another useful parameter that is not restricted to unidirectional waves is the input impedance Z_{in}, which is defined as the ratio of the pulsatile components of pressure and flow, and is a function of the angular frequency:

$$Z_{in}(\omega) = \frac{p(\omega)}{Q(\omega)} \tag{44}$$

Wave reflections

For tubes that are not infinitely long, straight, and cylindrical, the boundary conditions at the end of the tube have to be taken into account. In many cases waves will be reflected. Wave reflections occur when there is a change in the characteristic impedance [9, ch. 8]. A useful measure for the amount of wave reflections is the reflection factor Γ, defined by:

$$\Gamma = \frac{p_b}{p_f} = -\frac{Q_b}{Q_f} \tag{45}$$

where the subscript f denotes forward travelling waves and b backward travelling waves. The reflection factor can also be expressed in terms of the input impedance and the characteristic impedance:

$$\Gamma = \frac{Z_{in} - Z_c}{Z_{in} + Z_c} \qquad (46)$$

The terminal impedance $Z_T = \frac{p_{out}}{Q_{out}}$ can be used instead of the input impedance when looking at an outlet. Setting $\Gamma = 0$ gives a reflection free boundary.

2.2.6 Stationary Flow in Compliant Tubes

For laminar, fully developed pipe flow, Poiseuille flow is a valid simplification from the Navier-Stokes equations. Then the following relation between pressure gradient and flow is obtained [9, ch. 8]:

$$\frac{dp}{dx} = -\frac{8\pi\mu}{A^2}Q \qquad (47)$$

For a compliant tube the pressure can be substituted by the cross-sectional area, to give:

$$\frac{dA}{dx} = -C\frac{8\pi\mu}{A^2}Q \qquad (48)$$

Integration gives:

$$A(x)^3 = A(0)^3 - 24\pi\mu CQx \qquad (49)$$

or:

$$Q(x) = \frac{A(0)^3 - A(x)^3}{24\pi\mu Cx} \qquad (50)$$

so there is a non-linear relation between area and flow for compliant tubes. Using the simple constitutive model $A(p) = A_0 + C(p - p_0)$, a similar relation between pressure and area is obtained:

$$p(x) = p_0 + \frac{A(x) - A(0)}{C} \qquad (51)$$

or pressure and flow:

$$Q = \frac{A(0)^3 - (A(0) + C(p(x) - p(0)))^3}{24\pi\mu Cx} \qquad (52)$$

2.2.7 Windkessel Models

Windkessel models are examples of lumped models. In cardiovascular biomechanics this means that the physics of the entire systemic arterial system are represented by a few parameters [9, ch. 7]. The idea behind the Windkessel models is the similarity between the cardiovascular system and a fire hose. In a fire hose the pulsatile motion of the flow from the piston is damped by an air chamber (or Windkessel in German), so a continuous flow comes out of the hose. In the cardiovascular system the heart is the piston and the

large arteries are the air chamber. The compliance of the arteries damps the pulsatile motion of the flow so that it is almost completely smooth in the peripheral arteries.

The two-element Windkessel model was introduced by Otto Frank in 1899, as a mathematical model for such a system. Two parameters, a resistance R and a compliance C are included in this model. Later the model has been extended to include the characteristic impedance Z_c, in what is called the three-element Windkessel model. The two models are explained in more detail below.

Two-element Windkessel Model

The mathematical representation of the two-element Windkessel model is obtained by demanding mass conservation. For a large artery this can be written as:

$$Q = Q_a + Q_p \tag{53}$$

where Q is the flow into the artery, Q_p is the flow out of the artery, towards the periphery, and Q_a is the volume stored in the artery per time unit; the difference between inflow and outflow. Equation (53) can be written as a differential equation by introducing the peripheral resistance R and the total arterial compliance $C_V = \frac{\partial V}{\partial p}$, which describes how the volume V changes with the pressure [9, ch. 7]:

$$Q_a + Q_p = \frac{\partial V}{\partial p}\frac{\partial p}{\partial t} + \frac{p}{R} = C_V\frac{\partial p}{\partial t} + \frac{p}{R} \tag{54}$$

On a more standard form Eq. (54) can be written as:

$$\frac{\partial p}{\partial t} + \frac{p}{RC_V} = \frac{Q(t)}{C_V} \tag{55}$$

By expressing pressure and flow solutions as series of linearly independent Fourier modes, $p = \sum\limits_{n=0}^{N} p_n e^{j\omega_n t}$ and $Q = \sum\limits_{n=0}^{N} Q_n e^{j\omega_n t}$ and substituting into Eq. (55), an expression for the impedance of the two-element Windkessel model can be established [9, ch. 7]:

$$Z_n^{WK2} = \frac{R}{1 + j\omega_n RC_V} \tag{56}$$

with real part:

$$Z_{n,real}^{WK2} = \frac{R}{1 + (\omega_n RC_V)^2} \tag{57}$$

and imaginary part:

$$Z_{n,imag}^{WK2} = \frac{\omega_n R^2 C_V}{1 + (\omega_n RC_V)^2} \tag{58}$$

Three-element Windkessel Model

In addition to the peripheral resistance R and the total arterial compliance C_V, the three element Windkessel model has the characteristic impedance Z_c of the artery as a parameter. The characteristic impedance comes into the model by looking at the pressure drop between the inlet and a point downstream, which is given by:

$$p - p_d = Z_c Q \tag{59}$$

where p is the pressure at the inlet and p_d is the downstream pressure. The relation between p_d and Q is given by the two-element Windkessel model:

$$\frac{\partial p_d}{\partial t} + \frac{p_d}{RC_V} = \frac{Q}{C_V} \tag{60}$$

Substituting Eq. (59) into Eq. (60) gives the differential equation for the three-element Windkessel model [9, ch. 7]:

$$\frac{\partial p}{\partial t} + \frac{p}{RC_V} = \frac{Q}{C_V}(1 + \frac{Z_c}{R}) + Z_c \frac{\partial Q}{\partial t} \tag{61}$$

An expression for the impedance of the three-element Windkessel model can be established in a similar way as for the two-element Windkessel model. This gives:

$$Z_n^{WK3} = \frac{R + Z_c + j\omega_n RZ_c C_V}{1 + j\omega_n RC_V} \tag{62}$$

with real part:

$$Z_{n,real}^{WK3} = \frac{R}{1 + (\omega_n RC_V)^2} + Z_c \tag{63}$$

and imaginary part:

$$Z_{n,imag}^{WK3} = \frac{\omega_n R^2 C_V}{1 + (\omega_n RC_V)^2} \tag{64}$$

12

2.3 Solid Model

2.3.1 Governing Equations

The governing equation in solid mechanics is the Cauchy equation of motion, which is a differential form of the balance of linear momentum for a continuum. It is given by [9, p. 18]:

$$\rho \frac{d^2 \mathbf{u}}{dt^2} - \nabla \cdot \mathbf{T} = \rho \mathbf{b} \tag{65}$$

where $\mathbf{u}$ is the displacement vector, $\mathbf{T}$ is the stress tensor and $\mathbf{b}$ is a vector of body forces. A balance of angular momentum has to be fulfilled as well. This turns out to be true if:

$$T_{ij} = T_{ji} \tag{66}$$

where T_{ij} and T_{ji} are components of the stress tensor $\mathbf{T}$. For derivations see [9, p. 18].

While Cauchy's equation of motion relates forces to stresses, a kinematic condition is necessary to relate strains to displacements. For small deformations this can be expressed as follows:

$$E_{ij} = \frac{1}{2} \left(\frac{\partial u_i}{\partial x_j} + \frac{\partial u_j}{\partial x_i} \right) \tag{67}$$

where E_{ij} are the components of the Green strain tensor (not to be confused with the Young's modulus E).

2.3.2 Material Model

To close the system of equations for the solid model, a relation between stresses and strains is necessary. This relation depends on the material of the model and is called a constitutive relation. For an elastic material, stresses are functions of strains and particle coordinates only, and for a linear-elastic material this relation is linear. The most general constitutive equation for a linear-elastic material is given by:

$$\mathbf{T} = \mathbf{CE} \tag{68}$$

where $\mathbf{C}$ is a fourth order tensor of material constants. In the most general case, for a completely anisotropic material, the elastic tensor $\mathbf{C}$ has 36 independent constants (due to the symmetry of the stress and strain tensors, see Eq. (66), it is reduced from 81 to 36). For an isotropic linear-elastic material the number of independent constants is reduced to two; the Youngs modulus E and the Poisson's ratio ν. On matrix form, with index notation, Eq. (68) is then given by [10, ch. 7.2]:

$$T_{ij} = \frac{E}{1+\nu}\left[E_{ij} + \frac{\nu}{1-2\nu}E_{kk}\delta_{ij}\right] \tag{69}$$

2.4 Fluid-Structure Interaction Problems

A fluid-structure interaction problem (FSI) on a domain Ω, can be divided into a fluid subdomain Ω_f and a solid subdomain Ω_s, with boundaries Γ_f and Γ_s respectively, and the fluid-structure interface Γ_i. This is illustrated in figure 1. In the following, the subscript f denotes the fluid domain and s denotes the solid domain.
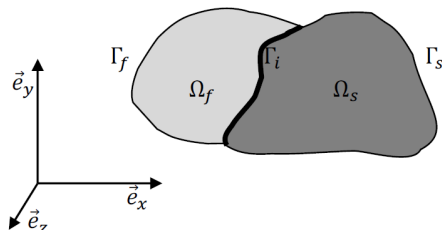

Figure 1: Illustration of the FSI problem domain. From [5].

For equilibrium at the fluid-structure interface the following kinematic and dynamic conditions have to be fulfilled at Γ_i [5]:

$$\mathbf{v}_f = \mathbf{v}_s = \frac{d\mathbf{u}_s}{dt} \tag{70}$$

$$\mathbf{T}_f \cdot \mathbf{n}_f = -\mathbf{T}_s \cdot \mathbf{n}_s \tag{71}$$

where $\mathbf{n}$ is a unit outward-pointing normal vector.

2.4.1 Lagrangian/Eulerian/ALE-frame

Structures are usually subjected to small displacements. When solving structural equations it is therefore reasonable to perform calculations with respect to the deformed configuration. This is called a Lagrangian formulation of the problem; a particle is followed when it moves in space. If instead of following the particle, a certain point in space is observed, an Eulerian formulation is used. This is the preferred method for fluids as they are subjected to large displacements, and it is the velocity field rather than the displacement field which is of interest. For fluid-structure interaction problems a compromise between an Eulerian and Lagrangian formulation is useful. It is problematic to use an Eulerian frame since the fluid domain

deforms with the compliant walls, but it is unnecessary to follow a fluid particle through the entire system.

An Arbitrary Lagrangian Eulerian (ALE) formulation is a reference frame where the computational domain moves with another velocity than the material. It is reasonable to choose the computational domain to move with the deforming walls.

2.4.2 Monolithic and Partitioned Solution Procedures

There are two approaches to solving an FSI-problem; a monolithic and a partitioned approach. A monolithic procedure solves the whole problem (fluid and solid) simultaneously in one solver. A partitioned solution procedure uses one solver for the fluid problem, another one for the solid problem and a coupling algorithm to perform iterations between the two problems.

Both approaches have their advantages and disadvantages. In a monolithic method the interaction can be taken into account during the solution process and no iterations have to be performed between the solution of structural and fluid equations. However, a global solver is needed so the software is usually less modular. A numerical scheme that is optimal for a fluid problem might not be as good for the solid case, and with a monolithic approach it is difficult to get optimized solvers for the entire problem. In a partitioned approach different software are used for the fluid and structure parts of the problem, so the numerical schemes may be optimized in each solver. But then again, great care have to be taken to maintain efficiency in the coupling algorithm, as several coupling iterations per time step are usually needed. Also, stability of the coupling scheme have to be considered, since not all coupling algorithms are unconditionally stable [7, p. 307] [5, p. 3].

2.4.3 Strong/Weak coupling (Implicit/Explicit)

In a strongly or implicitly coupled scheme Eqs. (70) and (71) are fulfilled after time discretization. Iterations are usually required to achieve this. In a weakly or explicitly coupled scheme, the structural and fluid equations are solved a fixed number of times in each time step, so equilibrium is not necessarily satisfied on Γ_i [7, p.307] [5, p. 12]. A monolithic approach is generally strongly coupled, while a partitioned approach can be either one.

Writing the flow solver as $\mathbf{y} = \mathbf{F}(\mathbf{x})$, where $\mathbf{y}$ represents the stress and $\mathbf{x}$ represents the displacement of the fluid-structure interface, and similarly the structural solver as $\mathbf{x} = \mathbf{S}(\mathbf{y})$, Degroote presents the most basic of the explicit schemes, also called the conventional serial staggered (CSS) scheme, as given in table 1 [5, p. 12].

The strongly coupled or implicit schemes enforce equilibrium on the fluid-structure interface with iterations in each time step. The most basic techniques uses Jacobi or Gauss-Seidel iterations between the fluid and

15

1.	Solve the flow equations $\mathbf{y}^{n+1} = \mathbf{F}(\mathbf{x}^n)$.
2.	Solve the structural equations $\mathbf{x}^{n+1} = \mathbf{S}(\mathbf{y}^{n+1})$.
3.	Go to the next time level.

Table 1: The conventional serial staggered (CSS) scheme. n indicates the time level.

structural solvers. As an example the Gauss-Seidel iteration scheme, also proposed by Degroote, is given in table 2 [5, p. 14].

1.	Solve the flow equations $\mathbf{y}^{k+1} = \mathbf{F}(\mathbf{x}^k)$.
2.	Solve the structural equations $\mathbf{x}^{k+1} = \mathbf{S}(\mathbf{y}^{k+1})$.
3.	**if** converged **then**
4.	Go to next time level.
5.	**else**
6.	Increase k and go to line 1.
7.	**end if**

Table 2: The Gauss-Seidel iteration scheme. k is the coupling iteration within a given time step n.

The schemes included here are only given to easily illustrate the difference between explicit and implicit coupling, and are not recommended in use. The CSS-scheme is only first order accurate in time and requires a smaller time step than the flow and structural solvers for stability. Implicit schemes with Jacobi or Gauss-Seidel iterations converge slowly or not at all. For more advanced coupling schemes, where these problems are avoided, see [5].

2.5 Numerical Solution Methods and Software

2.5.1 Computational Fluid Dynamics

"Computational fluid dynamics (CFD) is the analysis of systems involving fluid flow, heat transfer and associated phenomena such as chemical reactions by means of computer-based simulation" [14, p. 1]. The finite volume method (FVM) is the preferred method for space discretization in CFD today. In this method the governing equations are integrated over a control volume, and the integral form is discretized. This gives a clear physical interpretation of the problem [13] [14].

The FVM's success is based on its capability to capture shocks, that local grid adaption is possible, and its geometric flexibility, although it is not as good as the finite difference method (FDM) and finite element method (FEM) when it comes to higher orders of accuracy [13]. For the simulations in this study, the ANSYS 12.0 CFD-solver Fluent is used. Fluent uses FVM

to discretize the problem domain in space. The control volumes are cell-centered so they correspond directly with the mesh [3].

In Ansys several measurements of the mesh quality are available. The most general measure is the Element Quality which is based on a ratio between element volume and edge length. A value of 1 (best) indicates a perfect cube and 0 (worst) indicates zero or negative volume [1, p. 124]. Another important quality measure is the skewness of the mesh. This determines how close to equilateral or equiangular a cell or face is. In ANSYS the skewness quality parameter is a number between 0 and 1, where 0 (best) is an ideal cell/face and 1 (worst) is a completely degenerate cell. A value below 0.5 is considered good and below 0.25 excellent [1, p. 133].

2.5.2 Computational Structural Mechanics

For structural problems the finite element method (FEM), or finite element analysis (FEA), is the most popular solution method. In general it is a method for solving field problems numerically. FEM differs from FVM in that it approximates the field by piecewise interpolation of a field quantity, usually by polynomial interpolation, which gives a continuous field. Most types of finite elements are based on displacement fields. Values of the field quantity are calculated at nodes, which are points where elements are connected, loads are applied and boundary conditions are imposed [4].

For FEA there are no restrictions on geometry, loads or boundary conditions. Material properties need not be isotropic, and elements with different behaviour can be combined within one model. In this study the FEM-solver ABAQUS 6.11-1 is used.

2.5.3 Fluid-Structure Interaction

A partitioned approach is used to solve the FSI-problem in this study, with the in-house code Tango performing the coupling iterations between the fluid and structure solvers. An implicit coupling scheme called IQN-ILS (Interface quasi-Newton with a least-squares approximation of the inverse Jacobian) is employed. The algorithm is explained in depth by Degroote, [5, ch. 4.2.3], but a short presentation of the scheme is given in the following.

Previously the notation $\mathbf{y} = \mathbf{F}(\mathbf{x})$ and $\mathbf{x} = \mathbf{S}(\mathbf{y})$ has been used, where $\mathbf{y}$ represents the stress and $\mathbf{x}$ the displacement of the fluid-structure interface, and $\mathbf{F}$ and $\mathbf{S}$ the fluid- and structure solver respectively. Combining the expressions gives:

$$\mathbf{x} = \mathbf{S} \circ \mathbf{F}(\mathbf{x}) \tag{72}$$

or:

$$\mathbf{R}(\mathbf{x}) = \mathbf{S} \circ \mathbf{F}(\mathbf{x}) - \mathbf{x} = \mathbf{0} \tag{73}$$

where $\mathbf{R}(\mathbf{x})$ is the residual. Equation (73) is a non-linear system of equation and can be solved by Newton-Raphson iterations:

$$\mathbf{R}'^k \Delta \mathbf{x}^k = -\mathbf{r}^k \tag{74}$$

where:

$$\Delta \mathbf{x}^k = \mathbf{x}^{k+1} - \mathbf{x}^k \tag{75}$$

and:

$$\mathbf{r}^k = \mathbf{R}(\mathbf{x}) = \mathbf{S} \circ \mathbf{F}(\mathbf{x}^k) - \mathbf{x}^k = \tilde{\mathbf{x}}^{k+1} - \mathbf{x}^k \tag{76}$$

and $\mathbf{R}'^k$ is the Jacobian of $\mathbf{R}$ at $\mathbf{x}^k$. Iterations are run until a convergence criterion for the residual is fulfilled: $||\mathbf{r}^k||_2 \leq \epsilon_0$. An approximation has to be used for the Jacobian of $\mathbf{R}$ since the Jacobians of $\mathbf{F}$ and $\mathbf{S}$ are not available from the fluid- and structure solvers. In addition the Jacobian of $\mathbf{R}$ is usually dense, so there is a considerable computational cost of solving the Eq. (74) if there is a large number of degrees of freedom. With an approximation $\hat{\mathbf{R}}'$ for $\mathbf{R}'$ Eq. (74) can be written by means of quasi-Newton iterations as:

$$\mathbf{x}^{k+1} = \mathbf{x}^k + \left(\widehat{\mathbf{R}'^k}\right)^{-1}(-\mathbf{r}^k) \tag{77}$$

In the IQN-ILS method an approximation of the product between the inverse of the Jacobian and the residual, $\left(\widehat{\mathbf{R}'^k}\right)^{-1}(-\mathbf{r}^k)$, is calculated from information obtained during previous iterations. The details of how this is done can be found in [5]. An illustration of the scheme is given in figure 2. As for other quasi-Newton schemes, the IQN-ILS scheme will only converge if the initial guess is close enough to the final solution. If this is not the case the time step has to be adjusted.

2.6   Boundary conditions

In this study, the main concern is the boundary conditions at the outlet of a tube with one inlet and one outlet. These will be explained in detail in the following.

For velocity components at a solid wall the most appropriate boundary condition is usually the no-slip condition, $\mathbf{v} = 0$ [14, p. 273]. In the large arteries the wall is moving, so a corresponding condition is the kinematic condition given by Eq. (70). More advanced models might include the transfer of molecules from the blood into the wall in which case the velocity component normal to the wall is not zero. Advanced boundary conditions for the wall is outside the scope of this paper. For details see [7, p. 59].

A simple boundary condition for the structural boundary is to let the inlet and outlet expand freely in the radial direction, but not allow them to move lengthwise or rotate [6]. A more advanced model could take into
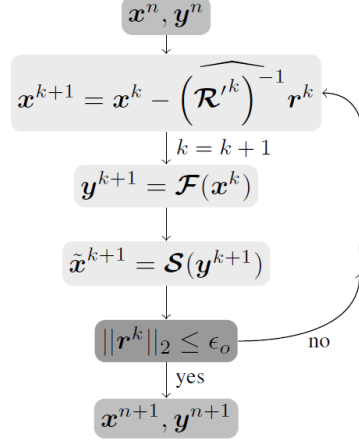
Figure 2: Representation of the IQN-ILS solution scheme. Collected from [5].

account the external tissue support at the outer wall, but this is also outside the scope of this paper. See [12] for details.

2.6.1 Reflection free outlet

To obtain a reflection free outlet, a pressure has to be imposed. The imposed pressure is obtained by setting the reflection factor in Eq. (46) equal to zero, and use the relation in Eq. (44). This gives:

$$p = Z_c Q \tag{78}$$

or on differential form:

$$\Delta p = Z_c \Delta Q \tag{79}$$

Using n to indicate the time level, Eq. (79) can be rewritten to:

$$p^n = p^{n-1} + Z_c(Q^n - Q^{n-1}) \tag{80}$$

2.6.2 Outlet with imposed reflections

To establish the imposed pressure for a boundary with reflections, a similar approach can be used as for a reflection free boundary. Equation (44) is substituted into Eq. (46) to give:

$$\Gamma = \frac{p - Z_c Q}{p + Z_c Q} \tag{81}$$

19

Rewriting Eq. (81) and writing it on differential form gives:

$$\Delta p = Z_c \frac{1 + \Gamma}{1 - \Gamma} \Delta Q \tag{82}$$

Using n to indicate the time level, this gives:

$$p^n = p^{n-1} + Z_c \frac{1 + \Gamma}{1 - \Gamma}(Q^n - Q^{n-1}) \tag{83}$$

2.6.3 Two-element Windkessel model at outlet boundary

To impose the two-element Windkessel model at the outlet, Eq. (55) is discretized with a backwards (implicit) Euler scheme:

$$p^n - p^{n-1} + \frac{\Delta t}{RC_V}p^n = \frac{\Delta t}{C_V}Q^n \tag{84}$$

where n indicates the time step. Rearranging to get an explicit expression for p^n gives:

$$p^n = \frac{1}{(1 + \frac{\Delta t}{\tau})}(p^{n-1} + \frac{\Delta t}{C_V}Q^n) \tag{85}$$

where $\tau = RC_V$ is a time constant. It can be shown that τ is the time it takes for the pressure to decrease to 37 % of the initial pressure, as the homogeneous solution of Eq. (55) is an exponential function $p = p_0 e^{-\frac{t-t_0}{\tau}}$ [9, ch. 7].

Estimations of R and C_V are needed to implement Eq. (85). Note that R is the resistance at the outlet and C_V is the total arterial compliance of the peripheral system, not the artery itself. Then R can be estimated as:

$$R = \frac{\bar{p}}{\bar{Q}} \tag{86}$$

where $\bar{p}$ is the mean pressure and $\bar{Q}$ is the mean flow through the artery. C_V can be estimated by using the definition of the time constant τ:

$$C_V = \tau/R \tag{87}$$

where τ should be chosen as a fraction of the period of the imposed pulse.

Another way to estimate the parameters R and C_V or τ is by using the real part of the expression for the impedance of the two-element Windkessel model, Eq. (57), substituting it for Z_{in} in the expression for the reflection factor, Eq. (46), and set $\Gamma = 0$. This gives:

$$R = Z_c(1 + (\omega\tau)^2) \tag{88}$$

and:

$$C_V = \frac{1}{\omega R}\sqrt{\frac{R}{Z_c} - 1} \tag{89}$$

2.6.4 Three-element Windkessel Model at outlet boundary

In a similar manner as for the two-element Windkessel model, the differential equation for the three-element Windkessel model, Eq. (61), can be discretized with a backwards Euler scheme to give:

$$p^n - p^{n-1} + \frac{\Delta t}{RC_V}p^n = \frac{\Delta t}{C_V}(1 + \frac{Z_c}{R})Q^n + Z_c(Q^n - Q^{n-1}) \tag{90}$$

Rearranging the equation to an explicit expression for p^n gives:

$$p^n = \frac{1}{(1 + \frac{\Delta t}{\tau})}[p^{n-1} + (\frac{\Delta t}{C_V}(1 + \frac{Z_c}{R}) + Z_c)Q^n - Z_c Q^{n-1}] \tag{91}$$

For the three-element Windkessel model, Z_c should be equal to the characteristic impedance of the tube, and can be calculated from Eq. (43). With Z_c known, R can be estimated as:

$$R = \frac{\bar{p}}{\bar{Q}} - Z_c \tag{92}$$

C_V can be determined in a similar manner as for the two-element Windkessel, Eq. (87). The parameters for the three-element Windkessel model can also be estimated from the setting the expression for the reflection factor, Eq. (46), equal to zero. Inserting the real part of the input impedance, Eq. (63), for Z_{in} gives:

$$R = 1 + (\omega\tau)^2 \tag{93}$$

and:

$$C_V = \frac{1}{\omega R}\sqrt{R - 1} \tag{94}$$

3 Method

All simulations were run on a computer consisting of one host (flukus) and two compute nodes (comp0 and comp1). Tango was run on the host. Fluent was run in parallel processing mode on one of the compute nodes (comp0). 6 Intel(R) Xeon(R), 3.00 GHz cpu's were used for the fluid calculations. Abaqus was run in parallel processing mode on the other compute node (comp1). 6 Intel(R) Xeon(R), 3.00 GHz cpu's were used for the structure calculations as well.

The absolute convergence criterion for the residual of the interface displacement was set to 10^{-6}, and for the load at the interface to 1 (see [2, p. 15]). The maximal number of coupling iterations per time step was 50. The convergence criterion for both continuity and momentum in Fluent was 10^{-6}, and the maximum number of iterations in fluent was 1000. In Abaqus the default convergence criteria were kept, and the maximum number of increments was set to 1000.

The geometry, meshes, material properties and boundary conditions for the different cases are presented in the following.

3.1 Geometry, Meshes and Materials

The geometry that was used was a straight tube, with the geometry used in [6]. The dimensions of the tube are given in table 3.

Dimensions [mm]	
Length	140
Inner diameter	20.5
Thickness	1.0

Table 3: Tube geometry

3.1.1 Computational Fluid Dynamics

The fluid meshes were created with the Ansys Meshing Application. The finest mesh consists of 29 046 6-noded wedge elements, with 16 815 nodes, a minimum element quality of 0.882 (on a scale where 0 is worst and 1 is best) and an average quality of 0.958. The mesh has a maximum skewness of 0.329 which is inside the limits of what is considered good quality, and an average skewness of 0.144, which is excellent. The mesh is shown in figure 3.

Two coarser fluid meshes were created to investigate the influence of grid refinement. The first, hereafter referred to as the medium mesh, consists of 13 608 6-noded wedge elements, with 8126 nodes, a minimum element quality of 0.929 and an average quality of 0.968. The mesh has a maximum
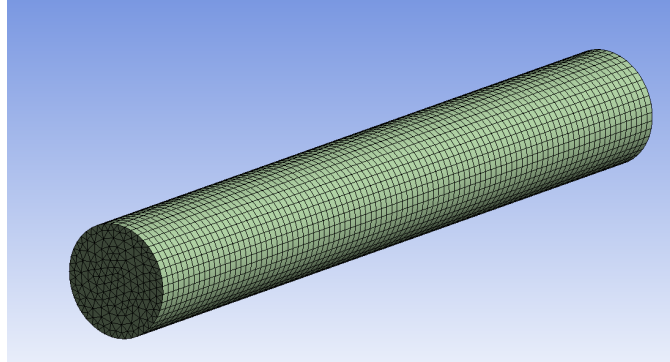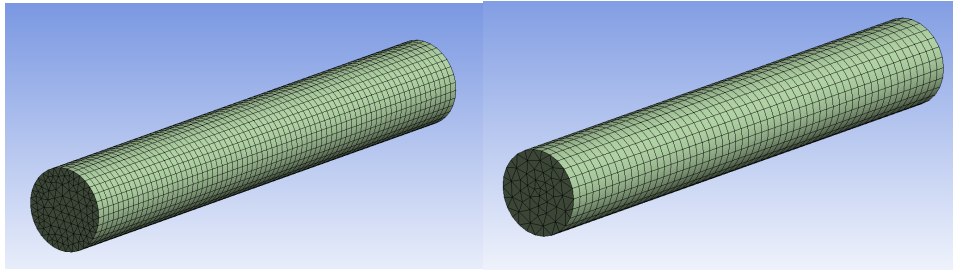
Figure 3: Fine fluid mesh

(a) Medium fluid mesh

(b) Coarse fluid mesh

Figure 4: Alternative fluid meshes

skewness of 0.241 and an average skewness of 0.13. The mesh is shown in figure 4a. The other, hereafter referred to as the coarse mesh, consists of 5472 6-noded wedge elements, with 3596 nodes, a minimum element quality of 0.619 and an average quality of 0.923. It has a maximum skewness of 0.484 and an average skewness of 0.18. The mesh is shown in figure 4b. A summary of the mesh data for the three meshes are given in table 4. The material properties of the fluid, collected from [11], is given in table 5.

Mesh	Fine	Medium	Coarse
Number of Elements:	29 046	13 608	5472
Number of Nodes:	16 815	8126	3596
Minimum Element Quality:	0.882	0.929	0.619
Average Element Quality:	0.958	0.968	0.923
Maximum Skewness:	0.329	0.241	0.484
Average Skewness:	0.144	0.130	0.180

Table 4: Mesh data for the fluid mesh

24

Parameter	Value
Density [kg/m^3]:	1050
Viscosity [Pa·s]:	$2.678 \cdot 10^{-3}$

Table 5: Material data for the fluid model

3.1.2 Structural Analysis

The mesh for the structure was created by Thomas Eeg for a master thesis written in 2012 [6]. Due to technical difficulties this mesh was used directly instead of creating a new one for this study. The mesh consists of 2300 8-noded, linear, hexahedral elements (C3D8), with 4692 nodes, and is shown in figure 5.
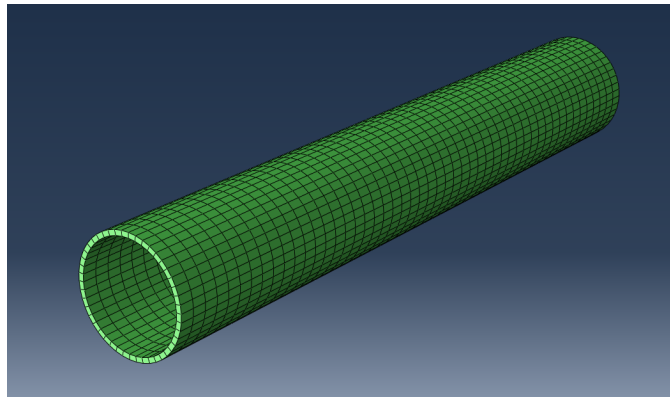

Figure 5: Structure mesh

The material parameters for the structure, collected from [11], is given in table 6.

Parameter	Value
Density [kg/m^3]:	1200
Poisson's ratio:	0.49
Young's modulus [Pa]:	$4.0 \cdot 10^5$

Table 6: Material data for the structure

3.1.3 Dependence on time step and grid refinement

When testing how the results would be influenced by changing grid size and time step, the following boundary conditions were used: A velocity was prescribed at the inlet and a pressure at the outlet. The velocity at the inlet was ramped up to a mean velocity of $v_0 = 0.2$ m/s during a time period of $t_r = 0.1$ s, where the shape of the ramp was given by a sine function:

$$v_{ramp} = v_0 \sin(\frac{\pi}{2} \cdot \frac{t}{t_r}) \tag{95}$$

The velocity was held constant at v_0 for $t_c = 0.15$ s, to give the flow time stabilize to stationary conditions, before a pulse with frequency of $f = 20$ Hz and an amplitude of $v_{amp} = 0.01$ m/s was imposed:

$$v_{pulse} = v_{amp} \sin^2(f\pi(t - (t_r + t_c)) + v_0 \tag{96}$$

A frequency of 20 Hz was chosen to be able to test for different time steps with a reasonable resolution of the pulse. At the outlet the pressure was ramped up to a mean pressure of $p_0 = 1333$ Pa (10 mmHg), in the same manner as the velocity:

$$p = R_0 Q \tag{97}$$

where $R_0 = \frac{p_0}{Q_0}$, Q is the flow and $Q_0 = v_0 A$ is the mean flow. When the velocity pulse was imposed at the inlet a reflection free pressure condition was applied at the outlet:

$$p^n = p^{n-1} + Z_c(\tilde{Q}^n - \tilde{Q}^{n-1}) \tag{98}$$

where $\tilde{Q} = Q - Q_0$, Z_c is the characteristic impedance of the flow and n indicates the time step. The Moens-Korteweg formula, Eq. (24), was used to calculate the wave speed. Initially both pressure and flow was zero. A no-slip condition was prescribed at the wall.

The inlet and outlet of the structure were allowed to move radially, but were constrained against movement and rotation in all other directions.

Simulations were run with the finest grid to investigate if the time step had an influence on the results. Four different time steps were tested, these are summarized in table 7.

Time step (Δt) [s]	Number of time steps
0.0015	270
0.0025	160
0.005	80
0.010	40

Table 7: Time steps for time step dependence tests. The fine grid was used in the simulations.

For the grid refinement tests a time step of 0.0025 s was used, to make sure that there weren't any loss of information due to too poor resolution in time. The simulations were run for 160 time steps.

3.1.4 Shell elements for the structure

To check if it was possible to use shell elements for the structure, and to see how it would influence the results, a quadrilateral mesh was created. The mesh consists of 2300 4-noded linear quadrilateral elements, with 2346 nodes; the same number of elements as for the hexahedral mesh. The mesh is shown in figure 6.

The same boundary conditions was used as when testing the influence of time step and grid refinement. The simulation was run with 160 time steps of 0.0025 s, and the medium fluid mesh was used.
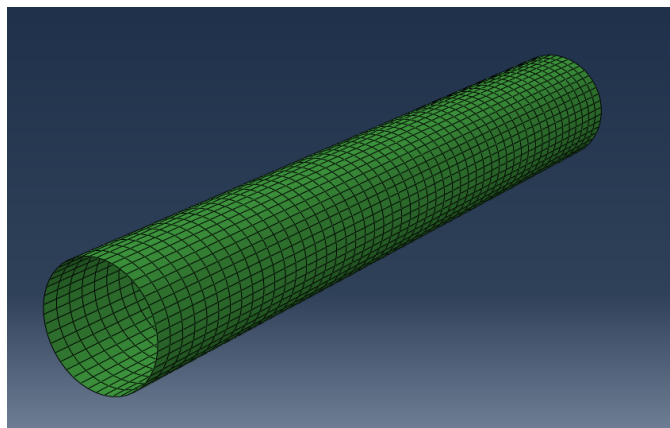

Figure 6: Structure mesh with quadrilateral (shell) elements

3.2 Boundary Conditions

3.2.1 Outlet with and without wave reflections

To investigate the effects of a reflection free boundary condition at the outlet, simulations were run in two steps:

1. CFD-analysis in Fluent through Tango.

2. FSI-analysis with Abaqus as the structural solver, Fluent as the fluid solver and Tango for the coupling.

Both the analyses were run with the same boundary conditions, time steps and mesh to be comparable. A FEM-analysis for the structure alone was performed to make sure the script files were correct, but the results are omitted in this paper, since a tube with constant internal pressure is a trivial case.

For the reflection free case, the same boundary conditions as earlier were used for the simulation, with the small change that the constant velocity/pressure state was held for 0.1 s longer, $t_c = 0.25$ s, as it was desirable

to look at the stationary state as well as the effects of the disturbance. Also, the frequency of the pulse was increased to $f = 80$ Hz, to make it easier to follow the pulse propagation through the tube and to avoid a reaction at the outlet before the entire pulse had left the inlet. The boundary conditions were then given by the following equations:

Inlet:

$$v = v_0 \sin(\frac{\pi}{2} \cdot \frac{t}{t_r}) \qquad t \leq t_r \qquad (99)$$

$$v = v_0 \qquad t_r < t < t_1 \qquad (100)$$

$$v = v_{amp} \sin^2(f\pi(t - (t_r + t_c))) + v_0 \qquad t_1 \leq t < t_2 \qquad (101)$$

$$v = v_0 \qquad t \geq t_2 \qquad (102)$$

where $t_1 = t_r + t_c$ and $t_2 = t_r + t_c + f^{-1}$. At the outlet the pressure was ramped up to a mean pressure of $p_0 = 1333$ Pa, in the same manner as the velocity, but with a linear instead of a sine-shaped ramp. The mean pressure was reached when the flow was equal to the mean flow. When the velocity pulse was applied at the inlet, the pressure was set to give a reflection free outlet:

$$p = R_0 Q \qquad t < t_1 \qquad (103)$$

$$p^n = p^{n-1} + Z_c(\tilde{Q}^n - \tilde{Q}^{n-1}) \qquad t \geq t_1 \qquad (104)$$

where $R_0 = \frac{p_0}{Q_0}$, $Q_0 = v_0 \cdot A$ and $\tilde{Q} = Q - Q_0$. Q_0 was recalculated each time step, since the area, A, changes with time. The simulations were run for 200 time steps of 0.0025 s.

To be able to see how a reflection free outlet behaves differently than one with reflections another FSI-simulation was run, where a reflection factor of $\Gamma = 0.9$ was imposed at the outlet. A CFD-analysis was not performed as wave reflections does not occur without the coupling with the structure. The following boundary condition was imposed for the pressure at the outlet:

$$p = R_0 Q \qquad t < t_1 \qquad (105)$$

$$p^n = p^{n-1} + Z_c \cdot \frac{1 + \Gamma}{1 - \Gamma}(\tilde{Q}^n - \tilde{Q}^{n-1}) \qquad t \geq t_1 \qquad (106)$$

All other parameters were the same as for the reflection free simulation.

It was also interesting to see how changing the velocity profile at the inlet affected the results for stationary conditions, especially when comparing the pressure gradient with that of a Poiseuille flow, Eq. (47). To do this, a parabolic velocity profile was imposed at the inlet. The velocity was ramped

up to a mean velocity of 0.2 m/s in a similar way as for previous simulations, and then held constant with respect to time for a long period, to give the flow time to reach a fully developed state. Only the stationary state was considered, so no velocity pulse was imposed.

$$v(r,t) = 2v(t) \cdot (1 - (\frac{r}{R})^2) \tag{107}$$

where R is the radius of the tube, and $v(t)$ is given by:

$$v = v_0 \sin(\frac{\pi}{2} \cdot \frac{t}{t_r}) \qquad t \leq t_r \tag{108}$$

$$v = v_0 \qquad t > t_r \tag{109}$$

The reflection free boundary condition was imposed at the outlet. The simulation was run for 270 time steps of 0.0025 s.

3.2.2 Two-element Windkessel model at outlet

The inlet boundary condition is the same uniform velocity condition as for the simulation with a reflection free outlet boundary, Eqs. (99) to (102). At the outlet the pressure was ramped up to a mean pressure of $p_0 = 1333$ Pa (10 mmHg) in a similar way as for previous simulations, but after the flow and pressure have reached a steady state, a pressure pulse given by Eq. (85) is added to the mean pressure. This gives the following boundary condition for the outlet:

$$p = R_0 Q \qquad t < t_1 \tag{110}$$

$$p^n = \frac{p^{n-1} - p_0 + \frac{\Delta t}{C_V} \tilde{Q}^n}{1 + \frac{\Delta t}{\tau}} + p_0 \qquad t \geq t_1 \tag{111}$$

where $R_0 = \frac{p_0}{Q_0}$, $Q_0 = 0.2 \cdot A$ and $\tilde{Q} = Q - Q_0$. Using Eqs. (86) and (87) to calculate the parameters R and C_V, and choosing a decay time τ to be half the period of the pulse, the numbers for the first case in table 8 are obtained.

Three additional cases were run, where the parameter R was chosen and C_V was estimated using equation (89). For the first one, a higher resistance than for the previous case was used, $R = 2.5 \cdot 10^7 \frac{\text{Pa} \cdot \text{s}}{\text{m}^3}$ and Eq. (89) was used to calculate C_V. The Z_c in Eq. (89) was calculated from Eq. (43) with A as the initial cross-sectional area of the tube. For the second, the same resistance as for the very first case was used, and C_V was calculated from Eq. (89), but here Z_c was calculated from the actual area of the outlet of the tube when the pulse passes. For the last case a lower resistance $R = 1.5 \cdot 10^7 \frac{\text{Pa} \cdot \text{s}}{\text{m}^3}$ was chosen, but the same procedure as for the previous case was used to calculate C_V. The parameters for the simulations are summarized in table 8. All simulations were run for 200 time steps of 0.0025 s.

Case	R $\left[\frac{\text{Pa}\cdot\text{s}}{\text{m}^3}\right]$	Z_c $\left[\frac{\text{Pa}\cdot\text{s}}{\text{m}^3}\right]$	C_V $\left[\frac{\text{m}^2}{\text{Pa}}\right]$	τ $[\text{s}]$
1	$1.9047 \cdot 10^7$	-	$3.28 \cdot 10^{-10}$	$6.25 \cdot 10^{-3}$
2	$2.5000 \cdot 10^7$	$1.3714 \cdot 10^7$	$7.2193 \cdot 10^{-11}$	$1.80 \cdot 10^{-3}$
3	$1.9047 \cdot 10^7$	$1.2767 \cdot 10^7$	$7.3255 \cdot 10^{-11}$	$1.40 \cdot 10^{-3}$
4	$1.5000 \cdot 10^7$	$1.2767 \cdot 10^7$	$5.5468 \cdot 10^{-11}$	$0.83 \cdot 10^{-3}$

Table 8: Parameters for the two-element Windkessel model. The Z_c given in the table was only used to calculate C_V, and is not one of the model parameters

3.2.3 Three-element Windkessel model at the outlet

The inlet condition was the same as for the two-element Windkessel model, Eqs. (99) to (102).

At the outlet the pressure was ramped up to a mean pressure of $p_0 = 1333$ Pa (10 mmHg) in a similar way as for the previous simulations. When a steady state was reached a pressure pulse given by Eq. (91) was added to the mean pressure. This gives:

$$p = R_0 Q \qquad\qquad t < t_1 \qquad (112)$$

$$p^n = (\frac{1}{1 + \frac{\Delta t}{\tau}})(p^{n-1} - p_0 + (\frac{\Delta t}{C_V}(1 + \frac{Z_c}{R}) +$$

$$+ Z_c)Q^n - Z_c Q^{n-1}) + p_0 \qquad t \geq t_1 \qquad (113)$$

where $R_0 = \frac{p_0}{Q_0}$, $Q_0 = 0.2 \cdot A$, $\tilde{Q} = Q - Q_0$, $\tau = RC_V$ and Z_c is the characteristic impedance of the tube.

Three different cases were run, with different numbers for the parameters R and C_V. In the first case Eq. (92) was used to estimate the resistance R and the total arterial compliance C_V was estimated using Eq. (87), where τ was chosen to be half the period of the imposed velocity pulse, $\tau = 0.00625$ s. For the second case the same R was used, but Eq. (94) was used to estimate C_V. This should theoretically give zero reflections. In the third case a higher resistance, $R = 1.5 \cdot 10^7 \frac{\text{Pa}\cdot\text{s}}{\text{m}^3}$ was chosen to see how this influenced the results. The total arterial compliance was estimated from Eq. (94). In all cases the characteristic impedance was recalculated for each time step, with A as the actual cross-section area of the tube, but for the first case the initial Z_c was used to estimate R. The simulations were run for 200 time steps of 0.0025 s. The parameters for the simulations are summarized in table 9.

Case	R $\left[\frac{\text{Pa·s}}{\text{m}^3}\right]$	Z_c $\left[\frac{\text{Pa·s}}{\text{m}^3}\right]$	C_V $\left[\frac{\text{m}^2}{\text{Pa}}\right]$	τ $[\text{s}]$
1	$5.333 \cdot 10^6$	$1.3714 \cdot 10^7$	$1.1719 \cdot 10^{-9}$	$6.25 \cdot 10^{-3}$
2	$5.333 \cdot 10^6$	-	$8.6148 \cdot 10^{-7}$	4.5943
3	$1.500 \cdot 10^7$	-	$5.1367 \cdot 10^{-7}$	7.7050

Table 9: Parameters for the three-element Windkessel model. The Z_c given here was used to calculate R in case 1, and was the initial Z_c used in the simulations. Z_c was recalculated each time step, since the cross-sectional area of the tube changes with time

4 Results and Discussion

In this chapter the results from all the cases that have been described will be presented and discussed. The cases are presented in the same order as in the previous chapter, starting with dependence on time step and grid refinement, and shell elements for the structure. Afterwards the simulations with focus on different boundary conditions are discussed, starting with CFD- and FSI-results from the reflection free case, before finishing with the results from the simulations with Windkessel models.

4.1 Dependence on time step and grid refinement

For the FSI-simulations that were run to test the dependence of time step, the fine mesh was used. The numbers and size of the time steps that were tested are given in table 7. For the grid refinement test the meshes presented in section 3.1.1 were used. The grid refinement test simulations were run for 160 time steps of 0.0025 s. A velocity pulse was prescribed at the inlet and a reflection free pressure condition at the outlet for all the simulations, as described in section 3.1.3.

The pressure, flow and area at the inlet and outlet of the tube are plotted against time in figure 7, for time steps 0.0025, 0.005 and 0.01. The simulation that was run with a time step of 0.0015 s is omitted in the plot as it would not converge. For both pressure and flow, changing the time step had almost no influence. The amplitude of the pulse was a bit less for larger time steps; this is probably because the dissipation increases when the time step and CFL-number increases. From the area plots it is clear that the area change at the inlet was influenced by the change in time step, but although there is a visible difference in the plot, the change was rather small. Changing the time step from 0.0025 s to 0.01 s gave an area change that was less than 1 % smaller, so this was not of any large concern. A small time step was still emphasized in further simulation, to get a good enough accuracy.

The influence of grid refinement was also very small, see figure 8. A coarser mesh gave slightly lower values for pressure, flow and area but the effect was not larger for the pulse than for the mean values, as was the case when increasing the time step. Since the difference was small, the medium mesh was used for further simulation, as this was the mesh with the highest quality, and it was more time efficient than using the fine mesh.

The CFL-numbers for the different test cases that were run are summarized in table 10. It is interesting to notice that although all the simulations were run with a maximum CFL-number much larger than one, it was only the ones with a time step 0.0015 s (or less, but these are not included in the table), that would not converge. To check if this had to do with the CFL-number or just the time step, a simulation was run on the coarse mesh with a time step of 0.002 s. This gave a lower CFL-number than for the
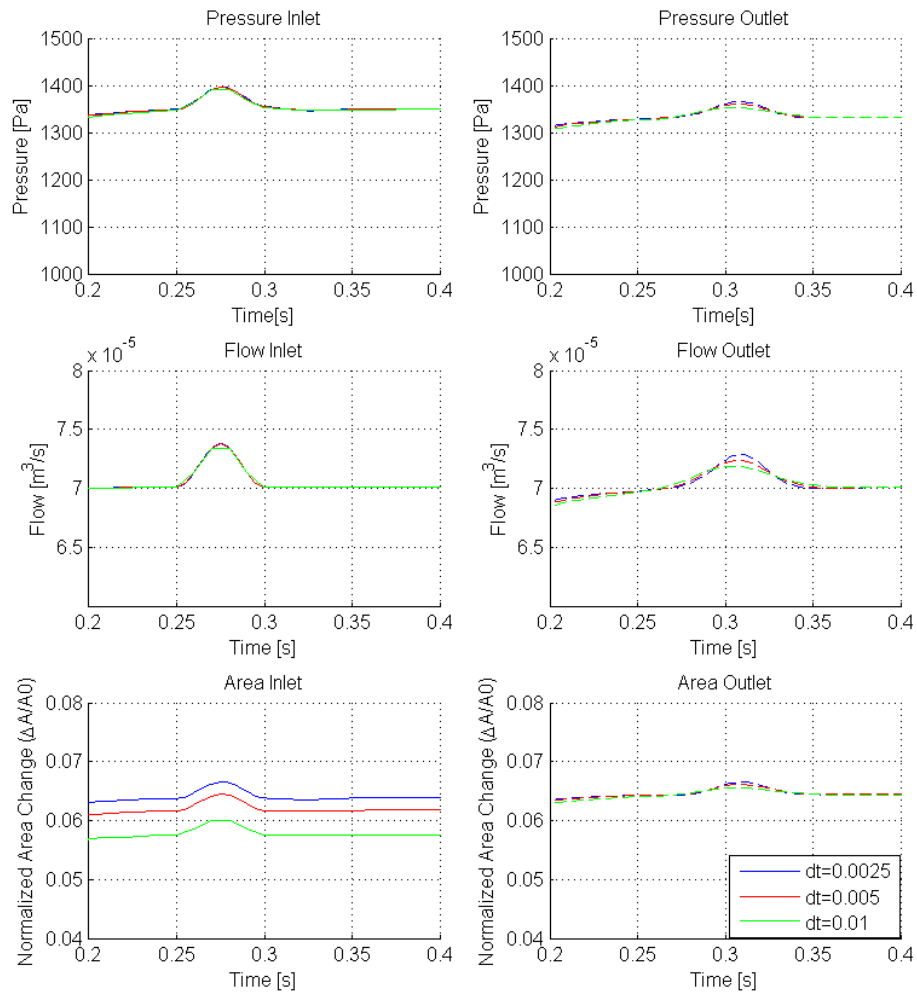
Figure 7: Results from time step dependence tests. Pressure, area, and flow at the inlet and outlet of the tube are plotted against time, for time steps 0.0025, 0.005, and 0.01. The fine grid was used in the simulations.
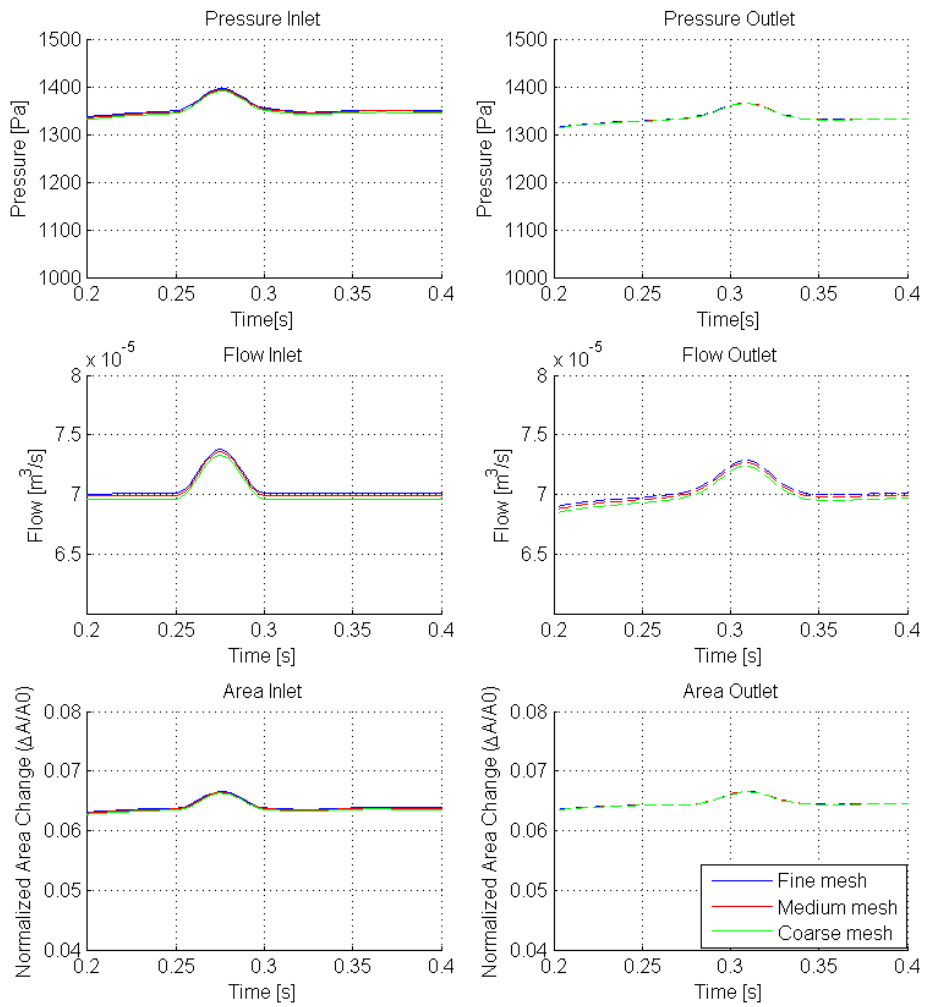
Figure 8: Results from grid dependence tests. Pressure, area, and flow at the inlet and outlet of the tube are plotted against time, for the fine, medium, and coarse grid. The simulation was run for 160 time steps of 0.0025 s; the first 0.2 s are omitted from the plots.

case with the fine grid and a time step of 0.0015 s, but this case converged, and the results were physical. It is therefore evident that the instabilities for low time steps are not linked to the CFL-numbers. Degroote mentions that FSI-simulations differs from other numerical problems in that decreasing the time step will in some situations increase the number of coupling iterations [5, p. 37]. Further he explains that for low wave numbers a small time step can give instabilities for a simulation where no coupling term is implemented [5, p. 49]. The details are omitted here, as it is outside the scope of this paper. A coupling term is implemented in the software used, so it is uncertain why oscillations still occur for small time steps, but there might be a connection here.

Mesh	dx_{min} [mm]	Δt [s]	CFL_{max}	Convergence?
Time step tests				
Fine	1.174	0.0015	5.51	No, oscillations
Fine	1.174	0.0025	9.18	Yes
Fine	1.174	0.005	18.4	Yes
Fine	1.174	0.01	36.7	Yes
Grid refinement tests				
Fine	1.174	0.0025	9.18	Yes
Medium	1.435	0.0025	7.51	Yes
Coarse	1.730	0.0025	6.23	Yes
Other tests				
Medium	1.435	0.0015	4.51	No, oscillations
Coarse	1.730	0.0015	3.74	No, oscillations
Coarse	1.730	0.002	4.98	Yes

Table 10: CFL-numbers for all test cases (grid refinement and time step dependence). $CFL = \frac{c_0 \Delta t}{\Delta x}$.

4.2 Shell elements for the structure

To test how using shell elements for the structure would influence the results, a simulation was run with the mesh shown in figure 6, see chapter 3.1.4. The same boundary conditions were used as when testing the influence of time step and grid refinement. The simulation was run with 160 time steps of 0.0025 s, and the medium fluid mesh was used.

The simulation would not converge. Convergence problems occurred in Fluent at time step 5, when the convergence criterion for continuity, 10^{-6}, was not reached. Changing the criterion to 10^{-3}, for easier convergence, did not solve the problem.

It is unlikely that using shell elements is the main reason for the problem with convergence. Several other hexahedral meshes was created, both for

the geometry described in this thesis and for a shorter tube. For some meshes the simulations would not converge and for some of the cases with the shorter tube a solution was obtained, but the results were non-physical; there were no signs of wave propagation. The problems seem to be related to mesh generation; Thomas Eeg also experienced similar problems in his thesis when using the same software [6].

A test case with a working mesh and a non-working mesh was sent to the developer of Tango, Joris Degroote, who was able to make it work with upgraded software. It is possible that upgrading to newer versions of Tango, Abaqus and Fluent will solve the problem.

4.3 Outlet boundary with and without wave reflections

In this chapter the results from the case described in chapter 3.2.1 are presented. The CFD-analysis with a reflection free outlet is discussed first, and afterwards both the FSI-simulation with a reflection free outlet and the FSI-simulation with an imposed reflection factor of $\Gamma = 0.9$.

4.3.1 CFD-analysis

The velocity and pressure at the inlet and outlet of the tube obtained from the CFD-analysis are plotted in figure 9. From figure 9b it is clear that the velocity at the outlet is the same as that imposed at the inlet. This is necessary for mass conservation since the cross-section area is constant along the tube. For the pressure it is interesting to compare the pressure gradient of the stationary flow to that of a Poiseuille flow, Eq. (47), and to compare the pressure gradient of the pulse to that of a one-dimensional transient flow, Eq. (9).

There are two requirements for Poiseuille flow; that the flow is laminar, and that it is fully developed. The Reynolds number for the flow, Eq. (7) is $Re = 1607.5$. It is less then the critical Reynolds number for transition to turbulence, $Re_{crit} \approx 2300$, so the requirement of laminar flow is fulfilled. However, the flow is not fully developed, so the flow profile does not agree with that of Poiseuille flow; the flow at the inlet of the tube is constant, while Poiseuille flow has a parabolic profile. Calculating the pressure difference between the inlet and outlet of the pipe from the results of the CFD-analysis at time t=0.3 s and for a similar Poiseuille flow, the numbers in table 11 are obtained. The pressure change is about three times larger than that for a Poiseuille flow, so it is clear that the assumption of such a flow is not valid. In addition to the flow not being fully developed, a reason for the difference could be that there might still be some transient effects present. The pressure has stabilized to a state where it does not change with time at t=0.3 s, but the simulation that is run is transient, not steady. The profile imposed at the inlet might not have had enough time to reach the outlet,

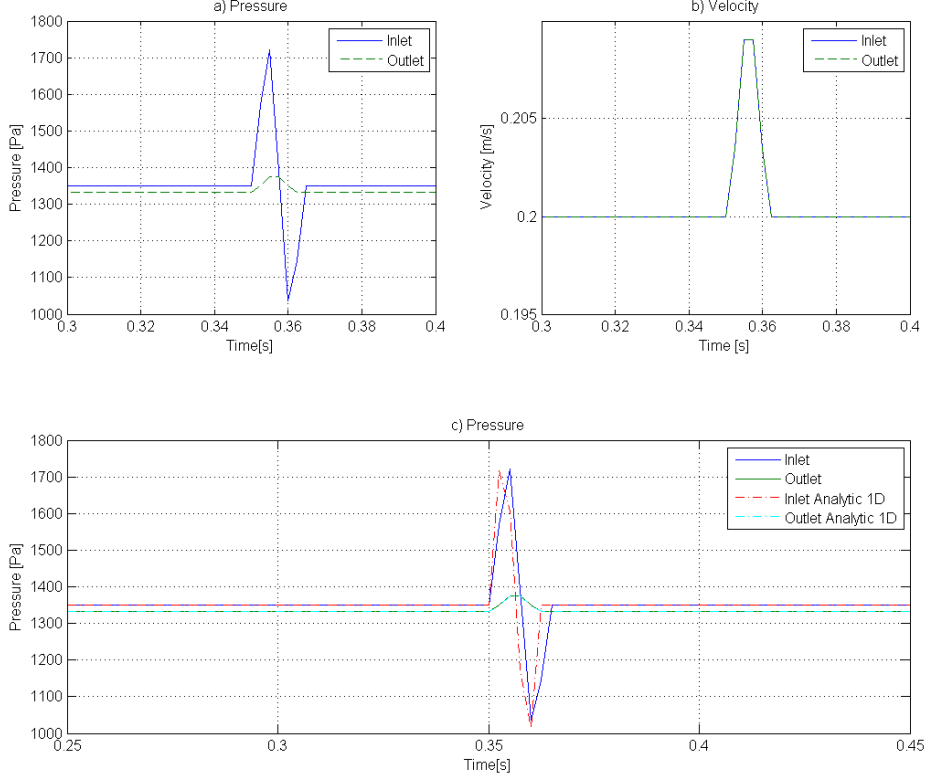which could also influence the pressure drop through the tube.

Figure 9: Results from the CFD-analysis. (a) Pressure and (b) velocity are plotted against time, and (c) the pressure is compared to the analytical solution, Eq. (10). The simulation was run with a uniform velocity profile at the inlet, and a reflection free pressure condition at the outlet, for 200 time steps of 0.0025 s.

Pressure Difference $\Delta p = p_{in} - p_{out}$ [Pa]	
CFD-analysis pressure difference:	17
Poiseuille flow theoretical pressure difference:	5.7

Table 11: Pressure difference between inlet and outlet for stationary conditions at t=0.3 s, from the CFD-results and from Eq. (47).

In figure 9c the pressure of the CFD-analysis solution is plotted together with the analytical solution for a one-dimensional transient tube, Eq. (10). This equation does not include the stationary pressure difference between inlet and outlet, but this is added in the plot to make it easier to compare the amplitude of the pulse. The stationary pressure difference added is that of the real flow $\Delta p = 17$ Pa, not that of a Poiseuille flow.

38

Pressure Amplitude [Pa]		
	$p_{max} - p_{mean}$	$p_{mean} - p_{min}$
CFD analysis:	371	313
Analytical 1D solution:	367	335.7

Table 12: Pressure pulse amplitude from the CFD-analysis and from the analytical solution, Eq. (10).

The agreement between the one-dimensional analytical solution and the three-dimensional simulated solution is very good, when it comes to the shape and the amplitude of the pressure pulse at the inlet. There is a small difference between the period of the pulse in the two cases, which is strange since the frequency is the same. It is uncertain why this happens, but it could have something to do with the time resolution of the pulse, which is quite low. The magnitude of the amplitude of the pressure pulse in both positive and negative direction is given in table 12. The small difference probably comes from the fact that the flow in the CFD-analysis is three-dimensional.

It is also interesting to note that Eq. (8), that is used to establish the analytical solution, is a version of Newton's 2nd law. The friction is negligible, so the large changes in pressure is solely due to the inertial effects of accelerating the mass of the fluid in the tube.

4.3.2 FSI-analysis

Several aspects are interesting to take a closer look at in the results of the FSI-simulations described in chapter 3.2.1:

- Is the outlet actually reflection free for the simulation where this is the imposed condition?

- Is the relationship between the amplitude of the pressure and flow pulse described by the characteristic impedance?

- Is the actual pulse wave velocity in agreement with the pulse wave velocity calculated from Moens-Korteweg formula, Eq. (24)?

- How does the stationary conditions agree with the equations for Poiseuille flow, Eqs. (50) and (51)?

- Is the damping of the pressure pulse from inlet to outlet in agreement with the theoretical damping coefficient, Eq. (37)?

A good way to see if the outlet is reflection free, is to compare the results of the reflection free simulation with the results from the case where a reflection factor of $\Gamma = 0.9$ was imposed. The results are compared by
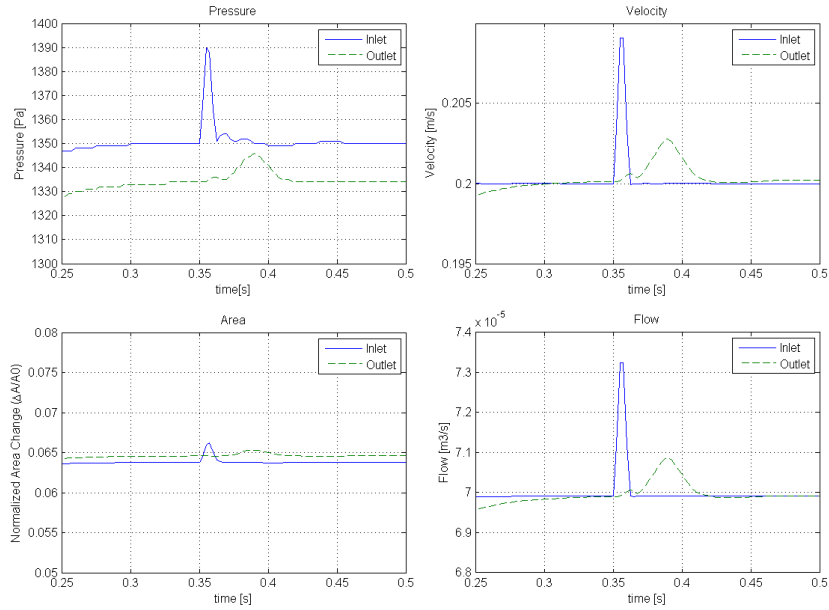
Figure 10: FSI results for a reflection free pressure outlet. A uniform velocity profile was imposed at the inlet. The simulation was run for 200 time steps of 0.0025 s. Pressure, velocity, area, and flow are plotted against time at the inlet and outlet of the tube. The ramp-up and stabilization of the flow for the first 0.25 s of the simulation are omitted.

the means of figures 10 and 11, and the pressure contour plots in figures 12 and 13. In figures 12 and 13 every 2nd time step is plotted, from $t = 0.3575$ s, when the peak of the pulse is observed at the inlet, until $t = 0.4225$ s, when the pulse is reflected back to the inlet for the first time in the case with reflections.

In figure 12, where the outlet boundary is reflection free, one can see that the pressure pulse travels through the tube during the first time steps, while for the last time steps nothing happen; a steady state is obtained. This means that the pulse is not reflected. In some of the time steps the pulse is barely visible, but this is because of the pressure gradient. The pressure plot in figure 10 shows that for the peak at the outlet the pressure is lower than the steady state pressure at the inlet, because the disturbance is quite small and it is damped while travelling through the tube as well.

In the case with reflections it is also hard to see the pulse for some of the time steps because of the pressure gradient, but the results are clearly different from the ones in the reflection free case. Also, there is a response at the inlet in the later time steps although no additional pressure or velocity
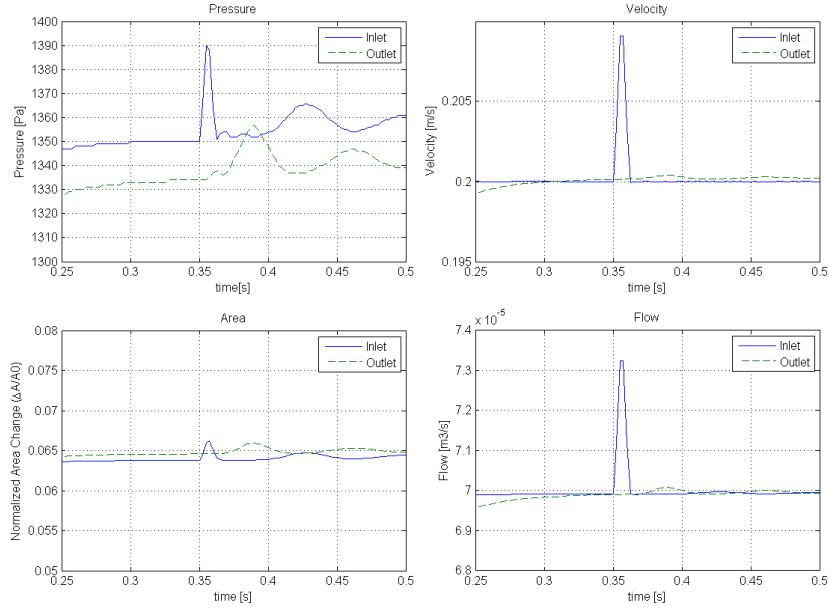
40

Figure 11: FSI results for a reflection factor of $\Gamma = 0.9$ at the outlet. A uniform velocity profile was imposed at the inlet. The simulation was run for 200 time steps of 0.0025 s. Pressure, velocity, area, and flow are plotted against time at the inlet and outlet of the tube. The ramp-up and stabilization of the flow for the first 0.25 s of the simulation are omitted.

changes are imposed there. This means that the pressure pulse, or at least parts of it, is reflected back through the tube. This is further illustrated by the oscillations of both pressure, flow and cross-sectional area, after the pulse is applied, in figure 11. No such oscillations are present i figure 10. It is therefore evident that the outlet is reflection free when that is the imposed condition.

The mathematical condition for a reflection free outlet is that $Z_c = p_{amp}/Q_{amp}$, where Z_c is given by Eq. (43) and p_{amp} and Q_{amp} are the amplitudes of the pressure pulse and flow pulse respectively. To make sure that this is fulfilled, the $\frac{Z_T}{Z_c}$-relation, where $Z_T = \frac{p_{amp}}{Q_{amp}}$ is plotted along the tube, for the cases with and without reflections in figure 14. Note that the amplitudes used in the plots are calculated at the time the pulse passes the given point in the tube, so it is plotted for a later time step at the outlet than the inlet, and not the same time step for the entire tube. Z_T in the case with a reflection free outlet almost coincides with the theoretical characteristic impedance, for the entire tube. In the case with imposed reflections at the
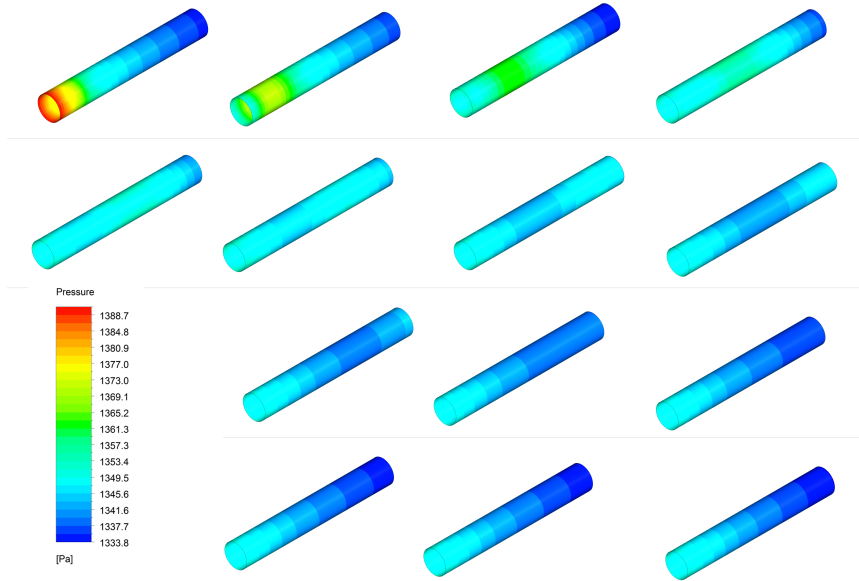
41

Figure 12: Pressure contours every 2nd time step from t=0.3575 s to t=0.4225 s for a reflection free pressure outlet
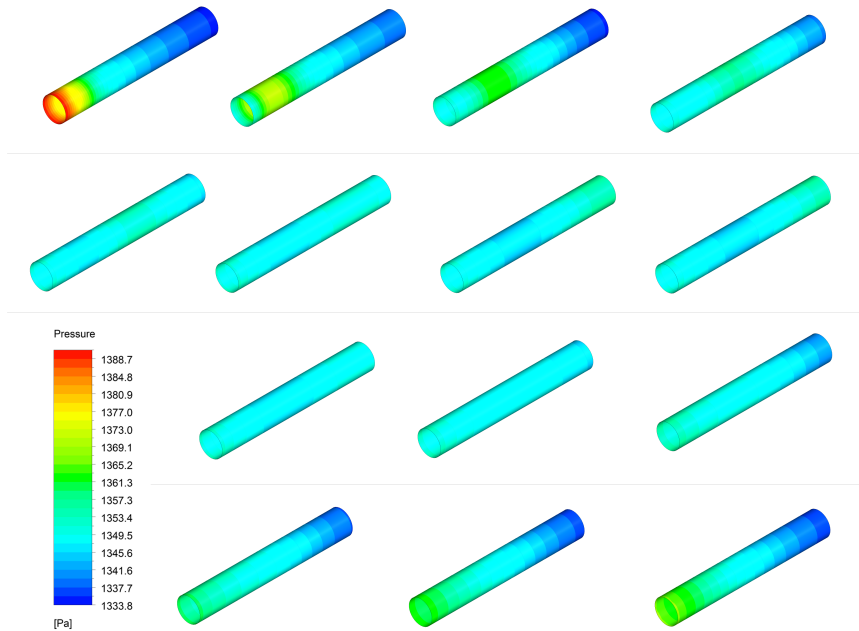

Figure 13: Pressure contours every 2nd time step from t=0.3575 s to t=0.4225 s for $\Gamma = 0.9$ at the outlet

outlet, Z_T is close to equal with the characteristic impedance through large parts of the tube. Near the outlet it is much larger, due to the large reflection factor.
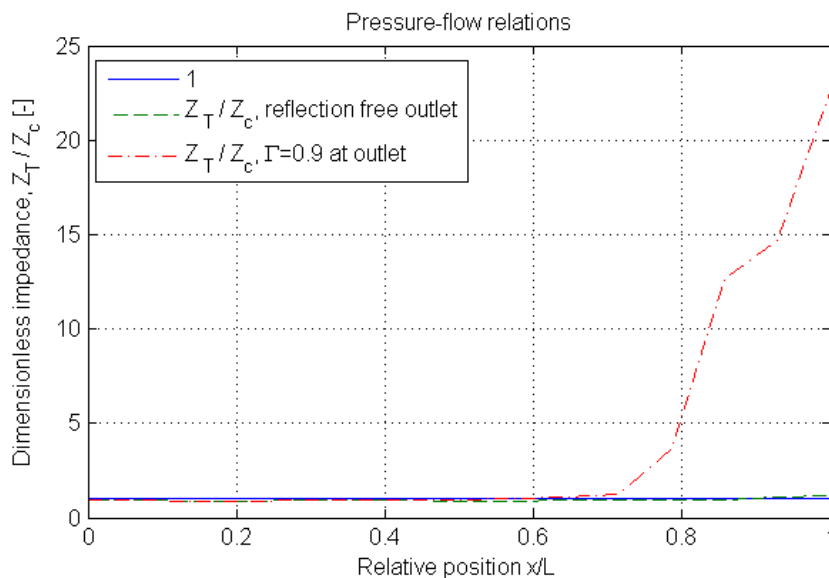

Figure 14: Plot of $\frac{Z_T}{Z_c}$ along the tube, for the FSI-simulations with $\Gamma = 0$ and $\Gamma = 0.9$ at the outlet. $Z_T = \frac{p_{amp}}{Q_{amp}}$. The amplitudes used for p_{amp} and Q_{amp} are calculated at the time the pulse passes the given point in the tube, so it is plotted for a later time step at the outlet than the inlet, and not the same time step for the entire tube.

Imposed reflection factor	Calculated reflection factor
0	0.0665
0.9	0.92

Table 13: Reflection factor at the outlet of the tube, calculated from the results of the FSI-simulations.

In table 13 the reflection factor calculated from Eq. (46), with $Z_T = p_{amp}/Q_{amp}$, is given at the outlet of the tube for both cases. There is a small amount of reflections at the outlet for the reflection free case. This does not show in figures 10 and 12 because the reflection factor is only 0.0665, so it is most likely damped away before it reaches the inlet. In the case where a reflection factor of $\Gamma = 0.9$ was imposed, the reflections are also very close to the prescribed value.

The Moens-Korteweg formula, Eq. (24), has been used to calculate the pulse wave velocity in all the computations. This equation gives a pulse

wave velocity of $c = 4.31$ m/s. Using data from the simulations to calculate the wave speed, by looking at the time it takes for the peak of the pressure pulse to travel from the inlet to the outlet, gives a pulse wave velocity of $c = 4.0$ m/s. Just looking at the numbers this seems like a large difference, but it turns out that if the pulse had used "one time step less" the simulation data would have given a wave speed of $c = 4.31$ m/s as well. This means that if the time step had been smaller, the pulse wave velocity of the flow would have been in even better agreement with the Moens-Korteweg pulse wave velocity.

Equations (50) and (51) can be used to calculate the theoretical pressure and flow at the outlet of a compliant tube for stationary condition. These values are given in table 14, where they are compared to the pressure and flow of the reflection free outlet simulation. The compliance C is calculated by using the definition of the pulse wave velocity and the Moens-Korteweg formula, Eq. (24). The pressure differences between the inlet and the outlet for stationary conditions, are given in table 15.

	Simulations		**Analytical solution**
	Inlet	Outlet	Outlet
Pressure [Pa]:	1350.0	1333.0	1332.18
Flow [m^3/s]:	$6.99 \cdot 10^{-5}$	$6.98 \cdot 10^{-5}$	$2.31 \cdot 10^{-4}$

Table 14: Pressure and flow through a compliant tube for stationary conditions at t=0.3 s, from the results of the simulation with a reflection free outlet and a uniform velocity profile at the inlet. The analytical solution is calculated from Eqs. (50) and (51).

Pressure Difference $\Delta p = p_{in} - p_{out}$ **[Pa]**	
FSI analysis pressure difference:	17.0
Pressure difference, equation (51):	17.8
Poiseuille flow theoretical pressure difference:	6.1

Table 15: Pressure difference between inlet and outlet for stationary conditions at t=0.3 s, from the results of the simulation with a reflection free outlet and a uniform velocity profile at the inlet. The values are compared to Eqs. (51) and (47).

The results in tables 14 and 15 show that the linear constitutive model for pressure as a function of area is a good approximation, but Eq. (50) can not be used to calculate the flow. This is because the assumption of Poiseuille flow, which Eq. (50) is based on, is not valid (see chapter 4.3.1). The same goes for the use of Eq. (47), the pressure gradient for Poiseuille flow, to calculate the pressure difference between the inlet and the outlet of

the tube, as is clearly illustrated by the numbers in table 15.

It should be noted that similar to the CFD-results, there could be transient effects present at t=0.3 s. The pressure and flow seem to have stabilized to a steady condition in figure 10, but the flow profile could still be changing throughout the tube and this would affect the pressure gradient. Still, if the pressure and flow had been kept constant for a longer time, to let the flow profile stabilize further, there would probably still be large differences between the pressure drop in the simulations and that for a Poiseuille flow. When a uniform profile is imposed at the inlet, the flow here will not change to the parabolic profile of a Poiseuille flow, so it will never be fully developed at the inlet.

Changing the velocity profile at the inlet to a parabola, Eq. (107), significantly improve the results when it comes to agreement with theoretical Poiseuille flow. The velocity profiles are plotted along the tube in figure 15. It is clear that the flow is fully developed at t=0.675 s. The pressure difference between the inlet and outlet when the flow is fully developed, at t=0.675 s, is 4.0 Pa; much closer to 6.1 Pa, than 17.0 Pa. The agreement is not complete, though. This could have to do with the compliance of the tube.
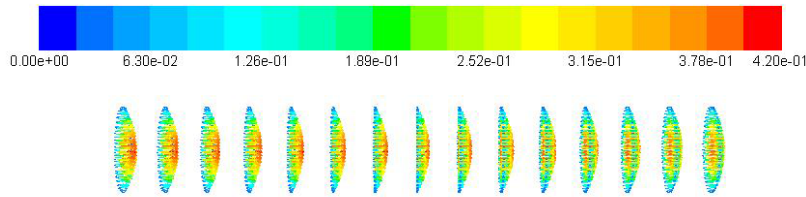

Figure 15: Velocity profiles through the tube for fully developed flow, at t=0.675 s. The result is from the simulation with a parabolic velocity profile at the inlet and a reflection free outlet boundary. The simulation was run for 270 time steps of 0.0025 s. No velocity pulse was imposed, just a ramp-up to a constant mean velocity.

There is a considerable amount of damping of the pressure and flow pulse through the tube. Using Eq. (37) the theoretical damping coefficient, γ_d, and the damping term, $e^{-\gamma_d x}$, can be calculated. The results are given in table 16. The amplitude of the pressure and flow pulse at the inlet and outlet is given in table 17.

The amplitude of the pressure pulse at the outlet is 32 % of that at the inlet, much less then the 99.7 % given by table 16. Again the problem is that derivation of the analytical solution of the wave equation with damping (chapter 2.2.5), is based on an assumption of Poiseuille flow. For real flows an empirical constant should be included in the expression for the

γ_d	$e^{-\gamma_d x}$
0.0216	0.9970

Table 16: Damping of the pulse between inlet and outlet, for the FSI-simulation with a reflection free outlet and a uniform velocity profile at the inlet

Inlet	Outlet
39.7	12.7

Table 17: Amplitude of the pressure pulse, for the FSI-simulation with a reflection free outlet and a uniform velocity profile at the inlet

shear stress, Eq. (14), which for this case is larger than one. More shear stress gives a larger amount of damping. There could be other effects that influence the results as well, but the non-validity of the Poiseuille flow assumption is definitively one of the more important.

The two outlet boundary conditions presented in this section illustrates the two extremes when it comes to wave reflections. This is useful to have in mind for the next cases, in which the results are probably somewhere in between.

4.4 Outlet boundary with two-element Windkessel model

For the two-element Windkessel model it is interesting to compare the results for different values of the parameters R and C_V, to see how these parameters influence the amount of wave reflections. The case discussed here is described in chapter 3.2.2. The parameters are summarized again in table 18 for the four cases, which from here on will be referred to with the case number in all figures.

Case	R	C_V	τ
	$[\frac{\text{Pa·s}}{\text{m}^3}]$	$[\frac{\text{m}^2}{\text{Pa}}]$	[s]
1	$1.9047 \cdot 10^7$	$3.28 \cdot 10^{-10}$	$6.25 \cdot 10^{-3}$
2	$2.5000 \cdot 10^7$	$7.2193 \cdot 10^{-11}$	$1.80 \cdot 10^{-3}$
3	$1.9047 \cdot 10^7$	$7.3255 \cdot 10^{-11}$	$1.40 \cdot 10^{-3}$
4	$1.5000 \cdot 10^7$	$5.5468 \cdot 10^{-11}$	$0.83 \cdot 10^{-3}$

Table 18: Parameters for the two-element Windkessel model

The pressure at inlet and outlet of the tube is compared for the four cases in figure 16. There seems to be a small amount of reflection for all cases, since the pulse comes back to the inlet, but with a much smaller amplitude.
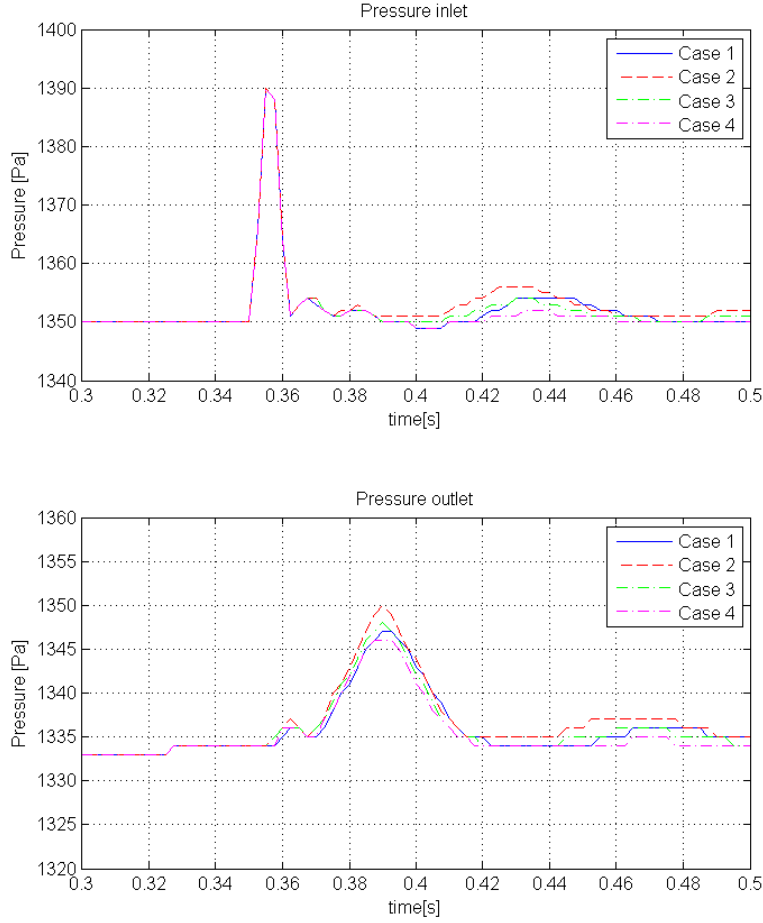
Figure 16: Comparison of pressure at inlet and outlet, plotted against time, for different parameters R and C_V. The results are from the FSI-simulation with a two-element Windkessel model at the outlet and a uniform velocity profile at the inlet. The simulation was run for 200 time steps of 0.0025 s.

There are differences in the results, though not very large. The amplitude of the pulse at the outlet increases as R increases, which is reasonable as a higher pressure is necessary to overcome a high resistance. The amplitude of the reflected pulse also increases with R. Physically this makes sense as well. The resistance can be seen as an obstacle that the pressure pulse has to pass. The part of the pulse that is not able to pass the obstacle will be reflected, so when resistance is increased the obstacle becomes harder to pass and a larger part of the pressure pulse will be reflected. The total arterial compliance of the peripheral system, C_V, seems to have a smaller

47

influence on the amount of reflections, and the same is the case for the algorithm used to estimate the parameters. Cases 2-4 should theoretically be free of reflections, while no such restrictions are applied to case 1. Still, the amplitude of the reflected pressure pulse is larger for case 2 than for case 1, since R is highest for case 2.
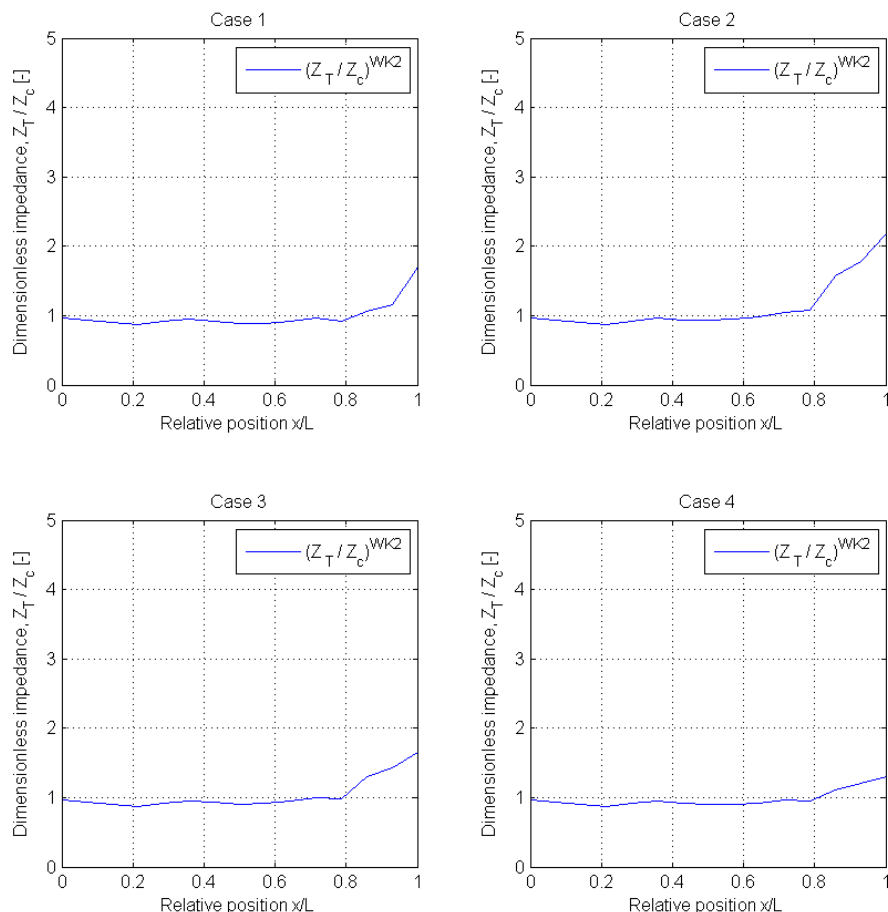

Figure 17: Plot of $\frac{Z_T}{Z_c}$ along the tube, for the FSI-simulations with the two-element Windkessel model at the outlet. $Z_T = \frac{p_{amp}}{Q_{amp}}$. The amplitudes used for p_{amp} and Q_{amp} are calculated at the time the pulse passes the given point in the tube, so it is plotted for a later time step at the outlet than the inlet, and not the same time step for the entire tube.

The amount of reflections becomes even clearer in figure 17, where the terminal impedance, $Z_T = \frac{p_{amp}}{Q_{amp}}$ is compared to the characteristic impedance. The amplitudes used in the plots are calculated at the time it passes a given point in the tube, so it is plotted for a later time step at the outlet than the inlet, and not the same time step for the entire tube. The theoretical

impedance at the outlet of the tube, Eq. (57), is calculated and compared to the characteristic impedance at the outlet in table 19. When it comes to Z^{WK2} and Z_c the disagreement is large for case 1, small for case 2, and there is a complete agreement in case 3 and 4. In case 1 no equality between Z^{WK2} and Z_c was demanded, so if there had been a better agreement this would have been a coincidence. In case 2, $Z^{WK2} = Z_c$ was used as a criterion, but the Z_c in Eq. (89) is based on the initial cross-sectional area of the tube, while the Z_c in table 19 is based on the actual area of the outlet when the pulse passes. This is enough to give a slightly higher impedance Z^{WK2} than Z_c. For the last two cases the Z_c in Eq. (89) is calculated in the same way as the plotted Z_c, so there is a complete agreement.

Case	Windkessel impedance (real part) $Z_{real}^{WK2} = \frac{R}{1+(\omega R C_V)^2}$	Characteristic impedance Z_c
1	$1.75 \cdot 10^6$	$1.28 \cdot 10^7$
2	$1.37 \cdot 10^7$	$1.28 \cdot 10^7$
3	$1.28 \cdot 10^7$	$1.28 \cdot 10^7$
4	$1.28 \cdot 10^7$	$1.28 \cdot 10^7$

Table 19: Impedance for the different cases of the two-element Windkessel model

From figure 17 it is clear that the agreement between the characteristic impedance and the terminal impedance from the simulations is rather poor at the outlet of the tube. As previously mentioned, reducing R reduces the pressure at the outlet. Figure 17 illustrates that this also reduces Z_T, as this quantity is largest for case 2, smaller for case 1 and 3, and smallest for case 4. In the last case the resistance was set to $R = 1.5 \cdot 10^7 \frac{\text{Pa} \cdot \text{s}}{\text{m}^3}$, and from the plot one can read that the terminal impedance is $Z_T = 1.67 \cdot 10^7 \frac{\text{Pa} \cdot \text{s}}{\text{m}^3}$ at the outlet, so it is a little higher than R. Decreasing R further would decrease Z_T to give an even better fit, and it seems like the optimal value would be $R = Z_c$. From Eq. (89) this would give a compliance of $C_V = 0$, which would reduce Eq. (85) to $p^n = p^{n-1}$. The two-element Windkessel model will therefore always give reflections.

Case	Theoretical reflection factor $\Gamma = \frac{Z^{WK2}-Z_c}{Z^{WK2}+Z_c}$	Actual reflection factor $\Gamma = \frac{Z_T-Z_c}{Z_T+Z_c}$
1	-0.7585	0.2590
2	0.0357	0.3719
3	0	0.2467
4	0	0.1322

Table 20: Reflection factor for the different cases of the two-element Windkessel model

The problem with reflections is highest for high frequencies. Equation (88) shows that increasing ω increases the difference between R and Z_c. The problem can in some degree be coped with by introducing a smaller τ, but it will always be present, and there will be disagreements between the theoretical reflection factor and the actual reflections. The reflection factors at the outlet of the tube are summarized for the different cases in table 20.

4.5 Outlet boundary with three-element Windkessel model

In the previous section it was shown that the two-element Windkessel model gives wave reflections for high frequencies even when it theoretically should be zero reflections. In this section the results from the simulations with a three-element Windkessel model at the outlet will be looked at to see if this is the case here as well. The case is described in chapter 3.2.3. The parameters that were used in the simulations are repeated in table 21, and the cases will from here on be referred to with case numbers in all figures.

Case	R	Z_c	C_V	τ
	$\left[\frac{\mathrm{Pa \cdot s}}{\mathrm{m}^3}\right]$	$\left[\frac{\mathrm{Pa \cdot s}}{\mathrm{m}^3}\right]$	$\left[\frac{\mathrm{m}^2}{\mathrm{Pa}}\right]$	$[\mathrm{s}]$
1	$5.333 \cdot 10^6$	$1.2767 \cdot 10^7$	$1.1719 \cdot 10^{-9}$	$6.25 \cdot 10^{-3}$
2	$5.333 \cdot 10^6$	$1.2772 \cdot 10^7$	$8.6148 \cdot 10^{-7}$	4.5943
3	$1.500 \cdot 10^7$	$1.2772 \cdot 10^7$	$5.1367 \cdot 10^{-7}$	7.7050

Table 21: Parameters for the three-element Windkessel model. The Z_c given here is calculated from the area of the outlet when the pulse passes. The initial Z_c that was used to calculate R in case 1 is $Z_c = 1.3714 \cdot 10^7 \frac{Pa \cdot s}{m^3}$.

In figure 18, the pressure at the inlet and outlet is plotted for different parameters R and C_V. The figure shows that the amount of reflections is seriously reduced when comparing with the two-element Windkessel. For the first case there was no restrictions on the amount of reflections, so the reflected pressure pulse is a bit higher here than for case 2 and 3, where there theoretically should be zero reflections. There is a complete overlap of the pressure curve for case 2 and 3, which indicates that changing R does not influence the results as long as C_V is calculated from equation (94).

In figure 19 the terminal impedance $Z_T = \frac{p_{amp}}{Q_{amp}}$ is compared to the characteristic impedance. The amplitudes used in the plots are calculated at the time it passes the given point in the tube, so it is plotted for a later time step at the outlet than the inlet, and not the same time step for the entire tube. The theoretical impedance at the outlet of the tube, Eq. (63), is calculated and compared to the characteristic impedance at the outlet in table 22. There is a small difference between the theoretical impedance Z^{WK3} and the characteristic impedance Z_c for case 1, but this could be because the initial characteristic impedance is used to estimate
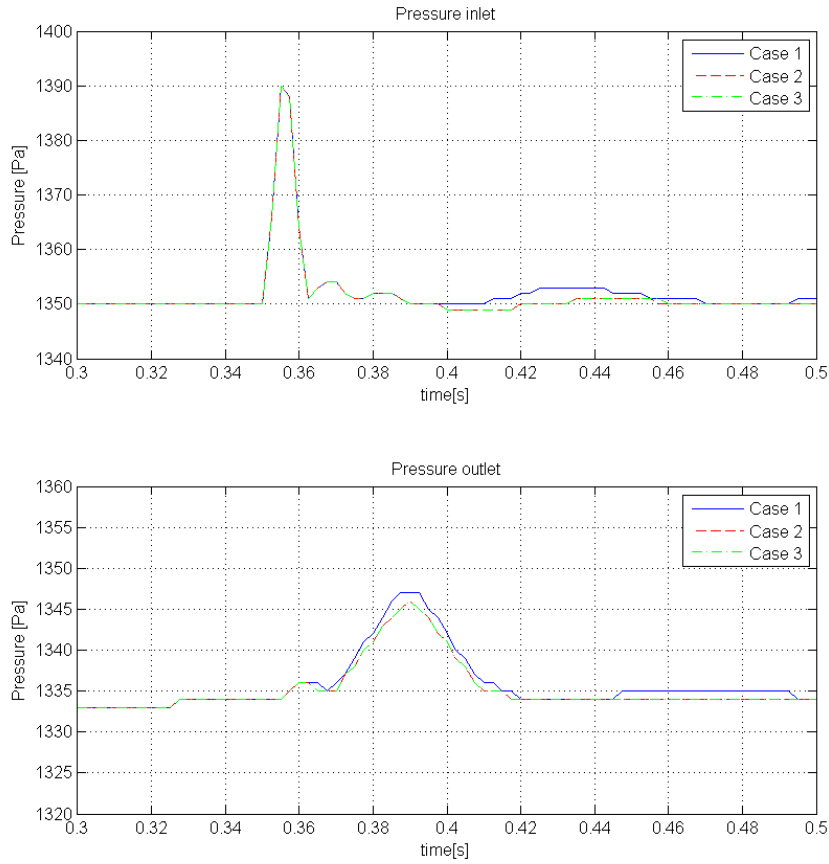
Figure 18: Comparison of pressure at inlet and outlet, plotted against time for different parameters R and C_V. The results are from the FSI-simulation with a three-element Windkessel model at the outlet and a uniform velocity profile at the inlet. The simulation was run for 200 time steps of 0.0025 s.

the resistance, Eq. (92), and the characteristic impedance in table 22 is calculated from the actual area of the outlet of the tube as the pulse passes. For case 2 and 3 there is a complete agreement between Z^{WK3} and Z_c. Also the difference between Z_T and Z_c at the outlet is very small for case 2 and 3 in figure 19.

Calculating the actual reflection factor and comparing it with the theoretical reflection factor, gives the numbers presented in table 23. For the simple reflection free case (see section 4.3.2) the reflection factor at the outlet was 0.0665. For case 2 and 3 presented here, the reflection factor is very close to this number. This indicates that the three-element Windkessel model is capable of modelling a reflection free outlet in the same degree as a simple reflection free model, if that is the restriction given when estimat-

ing the parameters. This is a very important property of the three-element Windkessel model contrary to the two-element Windkessel model.
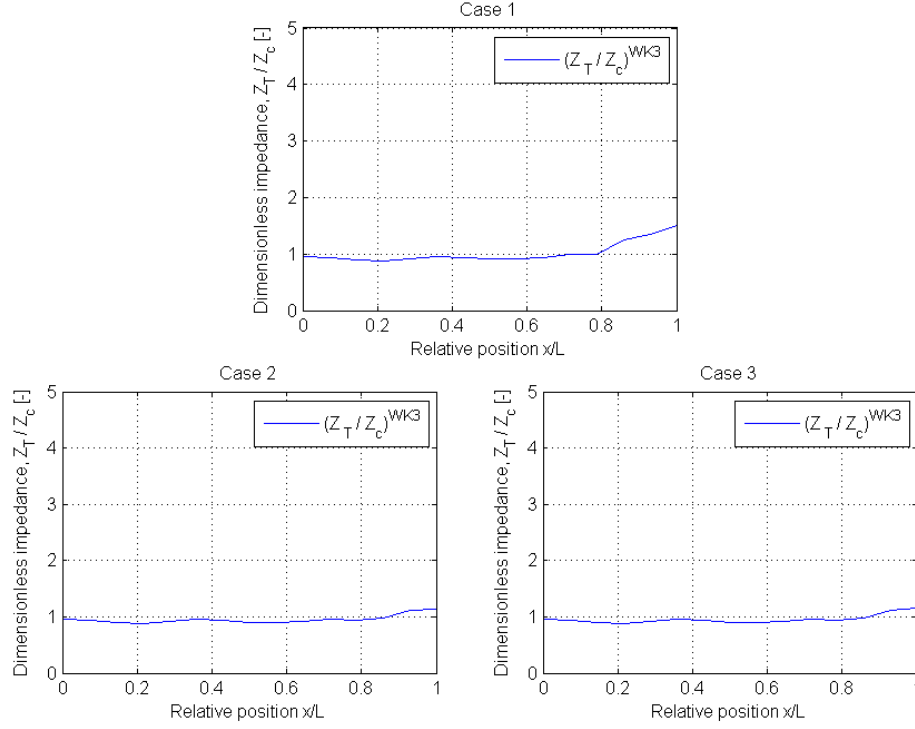
Figure 19: Plot of $\frac{Z_T}{Z_c}$ along the tube, for the FSI-simulations with the three-element Windkessel model at the outlet. $Z_T = \frac{p_{amp}}{Q_{amp}}$. The amplitudes used for p_{amp} and Q_{amp} are calculated at the time the pulse passes the given point in the tube, so it is plotted for a later time step at the outlet than the inlet, and not the same time step for the entire tube.

Case	Windkessel impedance (real part) $Z_{real}^{WK3} = \frac{R}{1+(\omega R C_V)^2} + Z_c$	Characteristic impedance Z_c
1	$1.33 \cdot 10^6$	$1.28 \cdot 10^7$
2	$1.28 \cdot 10^7$	$1.28 \cdot 10^7$
3	$1.28 \cdot 10^7$	$1.28 \cdot 10^7$

Table 22: Impedance for the different cases of the three-element Windkessel model

Case	Theoretical reflection factor $\Gamma = \frac{Z^{WK3}-Z_c}{Z^{WK3}+Z_c}$	Actual reflection factor $\Gamma = \frac{Z_T-Z_c}{Z_T+Z_c}$
1	0.0189	0.2033
2	0	0.0674
3	0	0.0682

Table 23: Reflection factor for the different cases of the three-element Windkessel model

5 Conclusion

A straight tube has successfully been used to test different boundary conditions, with focus on the outlet of the tube. In addition the dependence on time step and grid refinement was investigated.

Neither changing the time step size nor the grid size had any large influence on the results, but the simulations would not converge for very small time steps. This was not linked to the CFL-number. Increasing the grid size to get a lower CFL-number than for the simulations that did not converge was no problem, so this had only to do with the time step size. It is uncertain why this problem occurred, but it might have been related to the software, since an old version of Tango was used.

There were also some problems with mesh generation for the solid, probably in the conversion from Ansys Workbench mesh files to Abaqus input files. This was probably due to the old versions of the software, as the developer of the code managed to get it to work with the newest version of Tango. For future work, first priority should therefore be to update to the newest version of Tango, and perhaps also Abaqus and Fluent.

When it comes to boundary conditions, a simple reflection free model at the outlet was in high degree able to give reflection free results, though there were some minor reflections. This could have to do with the way $Z_T = \frac{p_{amp}}{Q_a mp}$ was calculated, when the mean pressure and flow was subtracted. It is not certain that the flow was entirely stabilized to stationary conditions when the pulse was imposed, and the mean pressure and flow was taken from values a few time steps before the pulse was applied. It is therefore possible that letting the flow stabilize for a longer time before imposing the pulse would give a more accurate estimation of the mean pressure. Another possibility would be to use a zero mean pressure and flow, but this is not a very good alternative, as the results would be highly non-physical. Since imposing reflections at the outlet gave a much higher amount of reflections than the reflection free condition, it is unlikely that it is the model itself that is the problem.

Using a uniform velocity profile at the inlet, makes the assumption of Poiseuille flow invalid. As a fully developed flow is a quite usual assumption when solving flow problems analytically, this makes it hard to validate results by comparing them to analytical solutions. Imposing a parabolic velocity profile, significantly improves the agreement between simulations and the analytical solutions for stationary conditions. Further investigations could be made to see how this influence the results for pulsatile flow as well.

The two-element Windkessel model is very inaccurate when it comes to modelling a reflection free outlet boundary. It is likely to be equally inaccurate when modelling imposed reflections. The results are significantly improved by upgrading to the three-element Windkessel model. The amount of reflections for a reflection free outlet with the three-element Windkessel

model was of the same size as for the simple reflection free model, so the small amount of reflections could probably be explained by the same inaccuracies.

A natural continuation of the work done in this study would be to look at more advanced boundary conditions at the inlet, since the focus in this study has been the outlet of a tube. With things working properly for a simple straight tube, more advanced geometry could be used as well. It could also be interesting to look at more physically accurate material models for both the structure and the fluid.

A one-dimensional network model for the peripheral arterial system has been developed in a previous study at NTNU. As an extension of the work with outlet boundary conditions, this could be coupled with the three dimensional FSI-modelling of the aorta.

References

[1] *ANSYS Meshing User's Guide 14.*

[2] *Tango Manual.*

[3] ANSYS FLUENT Training Materials. Introduction to ANSYS FLU-ENT 14, Lecture 1. `https://www1.ansys.com/customer/default.asp`, January 2012.

[4] Robert D. Cook, David S. Malkus, Michael E. Plesha, and Robert J. Witt. *Concepts and Applications of Finite Element Analysis.* John Wiley & Sons, 2002. Fourth edition.

[5] J. Degroote. *Development of Algorithms for the Partitioned Simulation of Strongly Coupled Fluid-Structure Interaction Problems.* PhD thesis, Ghent University, 2010.

[6] Thomas Bertheau Eeg. Fluid structure interaction simulation on an idealized aortic arch. Master's thesis, Norwegian University of Science and Technology, June 2012.

[7] L. Formaggia, A. Quarteroni, and A. Venezani (Editors). *Cardiovascular Mathematics, Modeling and simulation of the circulatory system. Volume 1.* Springer, 2009.

[8] Merethe SirevHansen. Fluid-structure interaction simulation on a simplified aortic arch. NTNU, 2012.

[9] Leif Rune Hellevik. Cardiovascular biomechanics. NTNU, 2012.

[10] Fridtjov Irgens. *Continuum Mechanics.* Springer, 2008.

[11] L. Lanoye. *Fluid Structure Interaction of Blood Vessels.* PhD thesis, Ghent University, 2007.

[12] P. Moireau, N. Xiao, M. Astorino, C. A. Figueroa, D. Chapelle, C. A. Taylor, and J.-F. Gerbeau. External tissue support and fluid-structure simulation in blood flows. *Biomech Model Mechanobiol*, 11:1–18, 2012.

[13] Bernhard Müller. Introduction to computational fluid dynamics, lecture notes. NTNU, 2011.

[14] H. K. Versteeg and W. Malalasekera. *An Introduction to Computational Fluid Dynamics, The Finite Volume Method.* Pearson Education, 2007. Second edition.

[15] Frank M. White. *Fluid Mechanics.* McGraw-Hill, 2008. Sixth edition.

[16] World Health Organization. Cardiovascular diseases (CVDs), Fact sheet N317. `http://www.who.int/mediacentre/factsheets/fs317/en/index.html`, May 2013.

Lists

List of Figures

List of Tables